REVIEWS

Quantum guidelines for solid-state spin defects

Gary Wolfowicz [1,2,12✉], F. Joseph Heremans [1,2,12], Christopher P. Anderson [2,3,12], Shun Kanai[4,5,6,7], Hosung Seo [8], Adam Gali [9,10], Giulia Galli [1,2,11] and David D. Awschalom [1,2,3]

Abstract | Defects with associated electron and nuclear spins in solid-state materials have a long history relevant to quantum information science that goes back to the first spin echo experiments with silicon dopants in the 1950s. Since the turn of the century, the field has rapidly spread to a vast array of defects and host crystals applicable to quantum communication, sensing and computing. From simple spin resonance to long-distance remote entanglement, the complexity of working with spin defects is fast increasing, and requires an in-depth understanding of the defects' spin, optical, charge and material properties in this modern context. This is especially critical for discovering new relevant systems for specific quantum applications. In this Review, we expand upon all the key components of solid-state spin defects, with an emphasis on the properties of defects and of the host material, on engineering opportunities and on other pathways for improvement. This Review aims to be as defect and material agnostic as possible, with some emphasis on optical emitters, providing broad guidelines for the field of solid-state spin defects for quantum information.

Defects in the solid state are at the centre of countless challenges and opportunities in condensed matter physics. They are either highly detrimental, for example, to crystalline growth, or beneficial, owing to their ability to modulate and control material properties. When isolated, impurities stand as analogues of atomic systems in an effective 'semiconductor vacuum'[1], with properties defined by the host substrate, leading to their study for first semi-classical and later quantum applications.

In 1958, electron spin resonance experiments were realized with phosphorus dopants in both natural and isotopically purified silicon, with the first spin-echo experiments[2] showing coherence times as high as 0.5 ms. In the 1960s, the first solid-state laser used chromium dopants in ruby[3], and many electron spin resonance experiments were realized in rare-earth ions in oxides[4]. It was not until the turn of the century, however, that a strong push for quantum applications started. This began with the proposal of quantum computers based on donors in silicon with electrical gates[5] or based on rare-earth ions in Y_2SiO_5 with optical cavities[6], and with the first measurement of single nitrogen-vacancy (NV) defects in diamond[7]. Following these successes, defects with spins in the solid state have rapidly been applied to all three major fields of quantum science: sensing, computing and communication. More recently, novel defects such as group IV dopant-vacancies in diamond[8] or

vacancy complexes in silicon carbide[9] have emerged and are especially promising for quantum communication.

Defects are defined by their spin, optical and charge states, as well as by the properties of their host material (FIG. 1). It is the interplay between all these components that allows complex experiments and technologies to be realized. Quantum sensing, for example, uses the spin state to acquire a phase shift from interactions with the environment[10], and an optical interface (that is, spin-to-photon conversion) allows optical readout of a spin qubit, potentially enhanced by spin-to-charge conversion[11]. Quantum computing is most closely realized with large clusters of nuclear spin registers coupled to an electron spin[12,13], alongside optical or charge-based control for efficient initialization and readout[14]. Quantum communications demand an efficient, spin-dependent optical interface[15] and a spin quantum memory[16].

In this Review, we broadly consider electron and nuclear spins associated with point defects primarily in bulk solid-state materials in the context of quantum science, with applicability to recent developments, including spins in 2D materials[17,18]. This scope encompasses single-atomic and atomic-vacancy defects, as well as vacancy complexes with magnetic, electrical, mechanical and optical interfaces for initialization, readout and control. The manuscript is divided into four main sections,

✉e-mail: gwolfowicz@anl.gov

covering spin properties, optical properties, charge properties and material considerations. We refer readers to other, more focused reviews for specific information on defects in diamond[8,19,20], silicon carbide[9,21], silicon[22], rare-earth dopants[23], theoretical modelling[24] and other aspects of solid-state spin defects[25–29].

Spin properties

For defects in the solid state, quantum information is generally encoded in the electron spin of the orbital ground state of the defect (with some exceptions[30]). Electron spins provide a controllable qubit with long relaxation and coherence times. They can be coupled to nuclear spins for long-lived quantum memories and advanced applications, such as quantum non-demolition (QND) measurements. Spin initialization, control and readout fidelities are critical parameters to optimize for all quantum applications. The spin state is, therefore, central to the quantum hardware and has been the subject of most theoretical and experimental research.

Spin relaxation. The spin relaxation time, T_1, is the characteristic time for the spin to reach an equilibrium state after random spin flips along the spin quantization axis. T_1 fundamentally limits the possible coherence time, T_2, such that $T_2 \leq 2T_1$, though, in practice, $T_2 \leq 0.5T_1$ or $1T_1$ (REFS[31,32]). The electron spin T_1 in the solid state, our focus here, is predominantly set by spin–lattice relaxation, namely, thermal relaxation from absorption, emission or scattering of phonons in the crystal through the spin–orbit interaction. This sets the operating temperature regime of the qubit, which is shown in FIG. 2a for common materials.

Predicting T_1 is challenging and requires ab initio computations of the spin-flip matrix elements from the spin–phonon interaction potential[33,34]. However, its dependence on various parameters such as the lattice temperature T_1 has been well described[35,36] and experimentally verified in many systems[37–39]. T_1 models are generally divided into three relaxation mechanisms (FIG. 2b): direct absorption or emission of one phonon resonant between two electron spin states, Raman processes by virtual absorption and emission of two phonons and Orbach[40] relaxation by phonon excitation to a

higher excited state, followed by decay and emission of a phonon.

For non-integer (Kramers) spins, T_1 follows[35,36]:

$$
\begin{aligned}
\frac{1}{T_1} \approx & \ K_D K_\theta \Delta E_{\text{spin}}^4 T \\
& + K_\theta^2 (K_{R1} T^5 + K_{R2} \Delta E_{\text{spin}}^2 T^7 + K_{R3} T^9) \\
& + K_O K_\theta \frac{\Delta E_{\text{orb}}^3}{\exp\left(\frac{\Delta E_{\text{orb}}}{k_b T}\right) - 1},
\end{aligned}
\tag{1}
$$

whereas for integer (non-Kramers) spins, T_1 follows:

$$
\begin{aligned}
\frac{1}{T_1} \approx & \ K_D K_\theta \Delta E_{\text{spin}}^2 T + K_\theta^2 (K_{R1} T^5 + K_{R2} T^7) \\
& + K_O K_\theta \frac{\Delta E_{\text{orb}}^3}{\exp\left(\frac{\Delta E_{\text{orb}}}{k_b T}\right) - 1}
\end{aligned}
\tag{2}
$$

where $K_\theta \propto \rho^{\frac{2}{3}}/\theta_D^5$ is a host-dependent parameter with ρ the atomic density and θ_D the Debye temperature, and K_D, K_{R1-3} and K_O are the coefficients for the direct, Raman and Orbach mechanisms, respectively, and are related to the spin–phonon coupling, in a way that is predictable from first principles[41,42]. ΔE_{spin} is the energy splitting between the ground spin states, ΔE_{orb} is the energy splitting (lower than the Debye frequency) between the ground and a nearby orbital excited state and k_b is the Boltzmann constant. Equations 1 and 2 are valid for $\Delta E_{\text{spin}}/k_b < T < \theta_D$.

For material design (FIG. 2c), the choice of the Debye temperature θ_D (via K_θ) has a large impact on the spin relaxation, especially for Raman processes ($\propto K_\theta^2$). For Raman processes, one power law generally dominates, such as T^9 in rare-earth ions[43]. The Orbach mechanism often dominates in the presence of a low-lying orbital state[39,43–45]. Furthermore, defects with highly spin-conserving orbital transitions can have long T_1 times, despite fast phonon absorption and excitation[46]. At extremely low temperatures ($\ll 1$ K), a phonon bottleneck effect can occur, in which there are not enough phonons to transfer energy from the spin to the lattice and the relaxation time is reduced[36,47]. Finally, the dependence on ΔE_{spin} for some of the mechanisms allows for tunability, usually using an external magnetic field[37].

The electron spin relaxation is not limited to phonon processes. Resonant magnetic or electric noise from the environment can effectively drive random flips of the defect electron spin[48,49]. In particular, this occurs near surfaces from dangling bonds[50,51] (see the section on spin coherence); in turn, monitoring T_1 can be used directly as a sensing mechanism[52,53]. Another decay pathway is via charge instability: in this case, the defect alternates between charge states in a non-spin-conserving manner[48]. Finally, undesired photoexcitation to an excited state followed by relaxation may cause spin flips similar to phonon-induced processes.

An isolated nuclear spin-1/2 in the solid state has very few direct phonon-mediated T_1 mechanisms. Its spin relaxation time is generally limited by coupling with the

Author addresses

[1]Center for Molecular Engineering and Materials Science Division, Argonne National Laboratory, Lemont, IL, USA.
[2]Pritzker School of Molecular Engineering, University of Chicago, Chicago, IL, USA.
[3]Department of Physics, University of Chicago, Chicago, IL, USA.
[4]Laboratory for Nanoelectronics and Spintronics, Research Institute of Electrical Communication, Tohoku University, Sendai, Japan.
[5]Division for the Establishment of Frontier Sciences, Tohoku University, Sendai, Japan.
[6]Center for Science and Innovation in Spintronics, Tohoku University, Sendai, Japan.
[7]Center for Spintronics Research Network, Tohoku University, Sendai, Japan.
[8]Department of Physics and Department of Energy Systems Research, Ajou University, Suwon, Gyeonggi, Republic of Korea.
[9]Wigner Research Centre for Physics, Budapest, Hungary.
[10]Department of Atomic Physics, Budapest University of Technology and Economics, Budapest, Hungary.
[11]Department of Chemistry, University of Chicago, Chicago, IL, USA.
[12]These authors contributed equally: Gary Wolfowicz, F. Joseph Heremans, Christopher P. Anderson
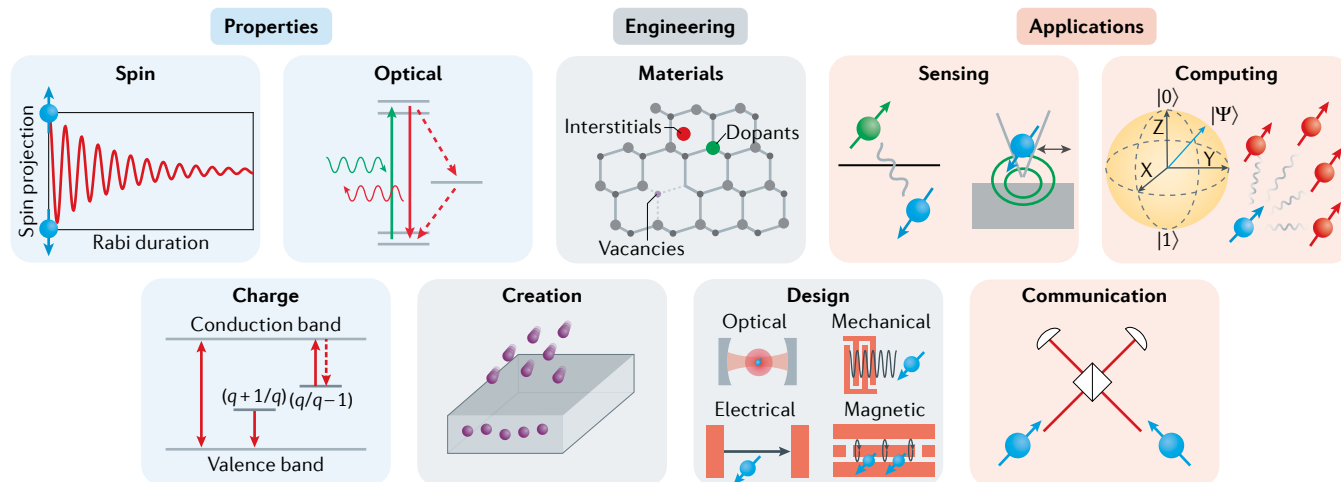
Fig. 1 | **Spin defects in the solid state for quantum information science.** Illustration of key concepts in the field, highlighting the three major defect properties (spin, optical and charge) in the blue panels, engineering considerations (materials, creation and design) in the grey panels and the three major quantum applications (sensing, communication and computing) in the red panels. For the properties, the panel on spin shows the spin projection during a Rabi oscillation; the panel on optical properties shows pumping (green) and photoluminescence (red) in a defect with an intersystem crossing; and the panel on charge shows transition energy levels for charge conversion. For the engineering considerations, the panel on materials displays various defect types and lattice sites; the panel on defect creation illustrates defect creation by implantation or irradiation; and the panel on design summarizes optical, mechanical, electrical and magnetic devices for interfacing with spin defects. Regarding the main applications of spin defects, the panel on sensing displays the use of the electron spin as sensor for other local spins or magnetic fields; the panel on computing shows the interaction of an electron spin with many nuclear spin registers; and the panel on communication shows entanglement between two spins via two-photon interference.

rest of the nuclear spin bath or with the electron spins in a sample. For the latter case, the nuclear spin T_1 is limited by cross-relaxation involving simultaneous electron and nuclear spin flips driven by phonon modulation of the hyperfine coupling[38]. In this case, the nuclear spin coherence may have an upper limit $T_{2,\text{nuclear}} \leq 2T_{1,\text{electron}}$ (REFS[16,54]), though this can be mitigated via dissipative decoupling[55].

The phonon-limited T_1 is one of the hardest characteristics to improve for a given temperature, defect and host material. However, the Orbach contribution can be reduced by increasing ΔE_{orb} through strain tuning[44], and engineering a phononic bandgap around ΔE_{spin} or ΔE_{orb} could eliminate either the direct or Orbach processes (FIG. 2d). Nanostructures smaller than the wavelength of relevant acoustic phonons could theoretically improve T_1 for spins, though they may suffer from surface proximity effects, and the required scales commonly exceed fabrication capabilities. Finally, lowering T_1 may be desired for spin polarization by thermal relaxation, and can be realized by Purcell enhancement of the spontaneous emission in a microwave cavity[56], which is normally negligible at microwave frequencies ($T_1^{\text{spont}} \approx 10^{17}$ s at 1 GHz (REF.[57])).

In summary, the electron spin relaxation time T_1 fundamentally limits the maximum electron (and sometimes nuclear) spin coherence time, and, therefore, all quantum applications. As a broad guideline, materials with high Debye temperature are preferred for qubit operation at elevated temperatures, especially for quantum sensing. Future challenges and opportunities involve controlling and increasing T_1 via the phononic density of states

(for defects limited by direct or Orbach processes), by theoretically predicting defects with specific electronic structures and by improving material quality to reduce resonant noise sources, especially near surfaces.

Spin coherence. Decoherence is the loss of phase information in a quantum system. Quantum applications require long coherence times for longer memories, higher control fidelities and longer phase acquisition times. Thankfully, decoherence can be well predicted and suppressed with sufficient knowledge of the quantum system and its environment. Typically, spin qubits lose their phase coherence, owing to surrounding fluctuating magnetic sources (that is, other nuclear and electron spins).

Coherence is characterized by two key figures: the inhomogeneous dephasing time $T_2^\star$ (measured by Ramsey interferometry) and the homogeneous dephasing time T_2 (measured by Hahn echo). In spin ensembles, $T_2^\star$ originates mainly from the random and (quasi-)static distribution of spin states and their interaction with the environment (bath). For single spins, $T_2^\star$ results mainly from experiment-to-experiment fluctuations in the spin bath state during averaging. In singles and ensembles, T_2 is obtained using a refocusing π pulse to suppress the static and slow fluctuations, and is, therefore, set by fast noise processes. In most relevant materials used for quantum applications, the electron spin $T_2^\star$ and T_2 are around a microsecond and a millisecond respectively, and can be extended to exceed seconds[32,58–60].

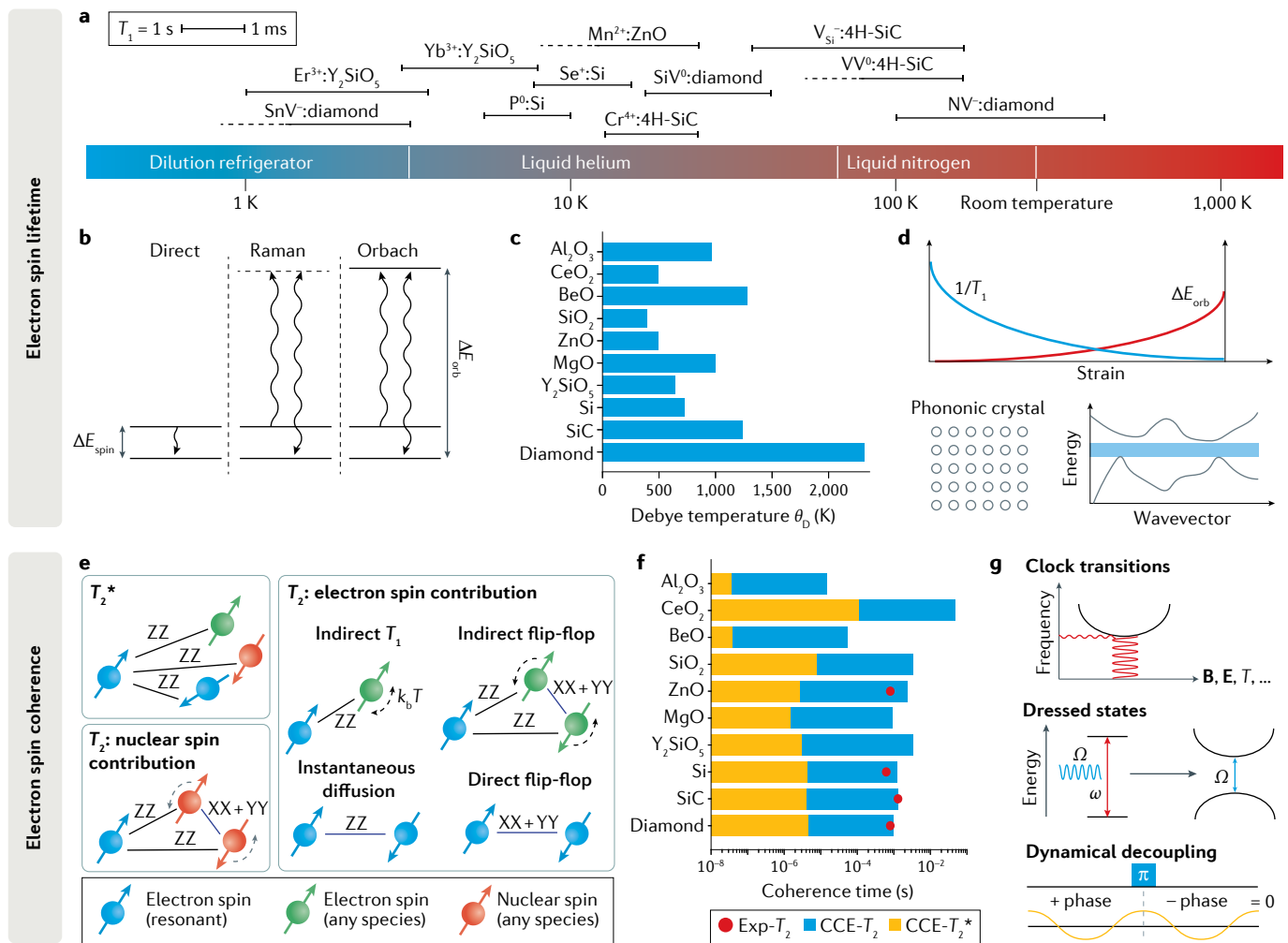In FIG. 2e, we consider the most common decoherence mechanisms for an electron spin in the solid state.

Fig. 2 | **Electron spin relaxation and coherence. a** | Temperature ranges corresponding to spin relaxation times, T_1, from 1 ms to 1 s in common defects for quantum information[38,142,175,222,255–261]. Dotted lines indicate parameters missing from the literature. **b** | Phonon processes for spin–lattice relaxation of electron spins in the solid state. ΔE_{spin} is the energy splitting between the ground spin states and ΔE_{orb} the energy splitting between the ground and a nearby excited state. **c** | Summary of Debye temperatures in relevant qubit host materials[262–266]. **d** | Engineering T_1 relaxation. Top: strain tuning of the ground-state orbital splitting can reduce the contribution of the Orbach process. Bottom: phononic structures can gap (in blue) relevant energies, such as ΔE_{orb} or ΔE_{spin}. **e** | Dominant decoherence mechanisms for an electron spin in the solid state. XX, YY and ZZ represent the interaction axes, with Z the quantization axis. T_2 and $T_2^{\star}$ are the homogeneous and the inhomogeneous dephasing times, respectively. **f** | Cluster correlation expansion (CCE) calculations of $T_2^{\star}$ and T_2 for a spin-1/2 electron spin coupled to a nuclear spin bath in various host materials with natural isotope abundance. The only defect-specific parameter used in the calculations is the standard gyromagnetic ratio $\gamma = 28\,GHz\,T^{-1}$. The hyperfine contact term is neglected, resulting in discrepancies between theoretical and experimental values for defects in silicon, for example. The red dots are experimental values for Mn²⁺:ZnO (REF.[255]) ($S = 1/2$), P⁰:Si (REF.[80]) ($S = 1/2$), VV⁰:4H-SiC (REF.[64]) ($S = 1$) and NV⁻:diamond[32] ($S = 1$), where the $S = 1$ systems have an expected ~20% variation from the $S = 1/2$ calculations. **g** | Hamiltonian engineering of the electron spin to create transitions insensitive to external fluctuations, such as magnetic field (**B**), electric field (**E**) or temperature (*T*) fluctuations. From top to bottom: clock transitions by static tuning of the spin interactions, dressed states for dynamical creation of clock transitions and dynamical decoupling for cancelling undesired phase accumulations. Ω, drive frequency; ω, spin transition frequency. Panel **e** is adapted with permission from REF.[267].

The naturally abundant non-zero nuclear spin isotopes of a material are often the dominant sources of magnetic field noise and can be readily simulated using fully quantum mechanical cluster correlation expansion (CCE) calculations[61,62]. From the spin Hamiltonian, one computes the coherence function $L(t) = \mathrm{Tr}[\rho(t)S^+]\,/\,\mathrm{Tr}[\rho(0)S^+]$ for an electron spin coupled to nuclear spins randomly distributed in the lattice, where t is the time, ρ is the density operator and S^+ is the electron spin raising operator. T_2 is then obtained from the decay profile $L(t) = \mathrm{e}^{-(t/T_2)^n}$ after ensemble averaging, with n the stretching exponent[63]. The density operator is approximated considering different orders of nuclear spin cluster sizes[64,65]. In FIG. 2f, we present cluster correlation expansion calculations[66] of predicted $T_2^{\star}$ and T_2 for relevant qubit host materials. There are three material factors that can reduce this decoherence contribution: a low abundance of non-zero nuclear spin isotopes, low nuclear gyromagnetic ratios and host lattices that prevent nearest-neighbour coupling of nuclear spins of the same species.

Semi-classical methods can also be used to predict coherence based on the random distribution (valid at low spin bath concentration C_B) of spin states in the

electron or nuclear spin bath. A coarse upper bound estimate for T_2^* is $1/R_{\text{dipolar}}$, with R_{dipolar} the characteristic dipolar coupling rate (in units of frequency)[57,67,68]:

$$R_{\text{dipolar}} = C_\text{B}(2\pi\gamma)(2\pi\gamma_\text{B})\frac{\pi}{9\sqrt{3}}\mu_0\hbar \qquad (3)$$

with γ and γ_B the measured and bath spin gyromagnetic ratios, respectively.

Surrounding electron spins start to significantly contribute to T_2 when their concentration reaches 10^{12}–$10^{14}\,\text{cm}^{-3}$, corresponding to coherence times below seconds[58]. First, 'instantaneous diffusion' occurs when the measured electron spin and other (usually electron) bath spins are simultaneously on resonance and evolve under a π pulse during a Hahn echo. In this case, the pulse has no refocusing effect and decoherence ensues like T_2^*, with $T_2 = 1/R_{\text{dipolar}}$ and, usually, $\gamma = \gamma_\text{B}$. Instantaneous diffusion rarely dominates in samples with isolated single spins, owing to the low concentration of resonant spins.

Magnetic fluctuations can also arise from the lifetime of electron spins in the bath, $T_{1,\text{B}}$. This 'indirect T_1' contribution to the decoherence follows the relation[58,57] $1/T_2 = \sqrt{R_{\text{dipolar}}/(2\pi T_{1,\text{B}})}$. Finally, the spin state exchange, or flip-flop, between resonant spins becomes relevant at higher spin concentration ($1/T_2 \propto C_\text{B}^2$)[69], though it can be suppressed by local detuning, such as magnetic field gradients. Flip-flops are either direct when involving the measured spin or indirect when only within bath spins. Direct flip-flop may contribute as a T_1 mechanism: if the state exchange includes a spin outside of the measured spin ensemble, or occurs for single spin measurements, then the spin projection information is lost after the spin flip[70].

Electric field noise can also be a major source of decoherence via modulation of certain spin parameters (see the section on spin control)[71–73]. Large electrical noise is rarely present in bulk materials and appears instead in nanoscale devices with metallic or highly doped regions, or near surfaces with dangling bonds[74]. T_2^* is also susceptible to static variations from strain in the crystal. Finally, decoherence can also occur through rapid thermal excitation/relaxation into an excited state with spin parameters different from those of the ground state[75].

An increase of coherence time can be engineered by reducing the nuclear spin bath density through isotopic purification[59,76–78] and by reducing the concentration of electron spins during crystal growth, defect creation and doping. Therefore, finding host materials in which this is possible is a key criterion for quantum information. Tuning the dimensionality (2D versus bulk) of the material can also improve decoherence, owing to the different spatial distribution of spins[79]. Similarly, for a dipole-coupled spin bath, the magnetic fluctuations can be suppressed for specific magnetic field orientations, depending on the host lattice structure[80].

In parallel, a defect's spin can be tuned to be less sensitive to its local environment by finding 'clock' (or zero first-order Zeeman[81]) transitions, or by dynamically creating a decoupled spin subspace, as illustrated in FIG. 2g. Clock transitions arise in systems with at least two competing spin interactions, such as Zeeman and hyperfine[59,82], or zero-field interactions[60,83], such that transition frequencies f become locally independent of a tunable or noisy parameter P, that is, $\text{d}f/\text{d}P \rightarrow 0$ (to first order). For a magnetic field, $P = B$, this gives an effective gyromagnetic ratio $\gamma_{\text{eff}} = \text{d}f/\text{d}B$ that reduces the interaction with the spin bath (and reduces R_{dipolar}, Eq. 3, for example)[84].

Whereas clock transitions passively decouple a qubit from its environment, the same decoupling effect can be obtained dynamically. Under a continuous resonant drive, the spin states are dressed and may form an avoided crossing split by the Rabi amplitude, with a local frequency minimum similar to that of a clock transition[85,86]. The drive can also be pulsed in a dynamical decoupling sequence. Dynamical decoupling is a generalization of the Hahn echo to arbitrary pulse sequences that cancel specific interactions with the environment[32,87], and is usually understood as a classical noise filter[88]. Unfortunately, decoupling techniques have limited effectiveness when correcting for strong or resonant noise, where homogeneous and inhomogeneous errors in drive frequency or amplitude are present, and may cause drive-induced heating[89].

In summary, limitations in the electron spin coherence times T_2^* and T_2 originate mainly from either magnetic field fluctuations from the nuclear spin bath, which can be mitigated using host materials with low spin-full isotope concentrations, or from high electron spin densities, which can be reduced by improving material quality. The coherence times can be accurately predicted using cluster correlation expansion calculations and intuitively understood using semi-classical models, guiding wide explorations for better host materials. They can be further improved using clock transitions, dressed states or dynamical decoupling (for low control errors), enabling high-sensitivity quantum sensing and long-lived quantum memories.

Spin control. A large variety of protocols are available to coherently control the electron (or nuclear) spin state[25]. These schemes include optical, magnetic, electric and strain fields, each with advantages and disadvantages, depending on the specific electron spin and orbital level structures of the defect, and the application at hand.

An electron spin ($\mathbf{S}$) coupled to a nuclear spin ($\mathbf{I}$) can be described by the following spin Hamiltonian:

$$H = \underbrace{\mu_\text{B}\mathbf{B} \cdot \mathbf{g_e} \cdot \mathbf{S}}_{\text{electron Zeeman}} + \underbrace{\mathbf{S} \cdot \mathbf{D} \cdot \mathbf{S}}_{\text{zero–field}} \\ - \underbrace{\mu_\text{N}\mathbf{B} \cdot \mathbf{g_n} \cdot \mathbf{I}}_{\text{nuclear Zeeman}} + \underbrace{\mathbf{S} \cdot \mathbf{A} \cdot \mathbf{I}}_{\text{hyperfine}} + \underbrace{\mathbf{I} \cdot \mathbf{Q} \cdot \mathbf{I}}_{\text{quadrupole}} \qquad (4)$$

where each bracket denotes a different spin interaction parameterized by the external magnetic field ($\mathbf{B}$), the electron and nuclear spin g-tensor ($\mathbf{g_e}, \mathbf{g_n}$), the zero-field splitting tensor for $S > 1/2$ ($\mathbf{D}$), the hyperfine coupling tensor ($\mathbf{A}$, including both contact and dipolar terms) and the quadrupole tensor for $\mathbf{I} > 1/2$ ($\mathbf{Q}$)[57]. μ_B and μ_N
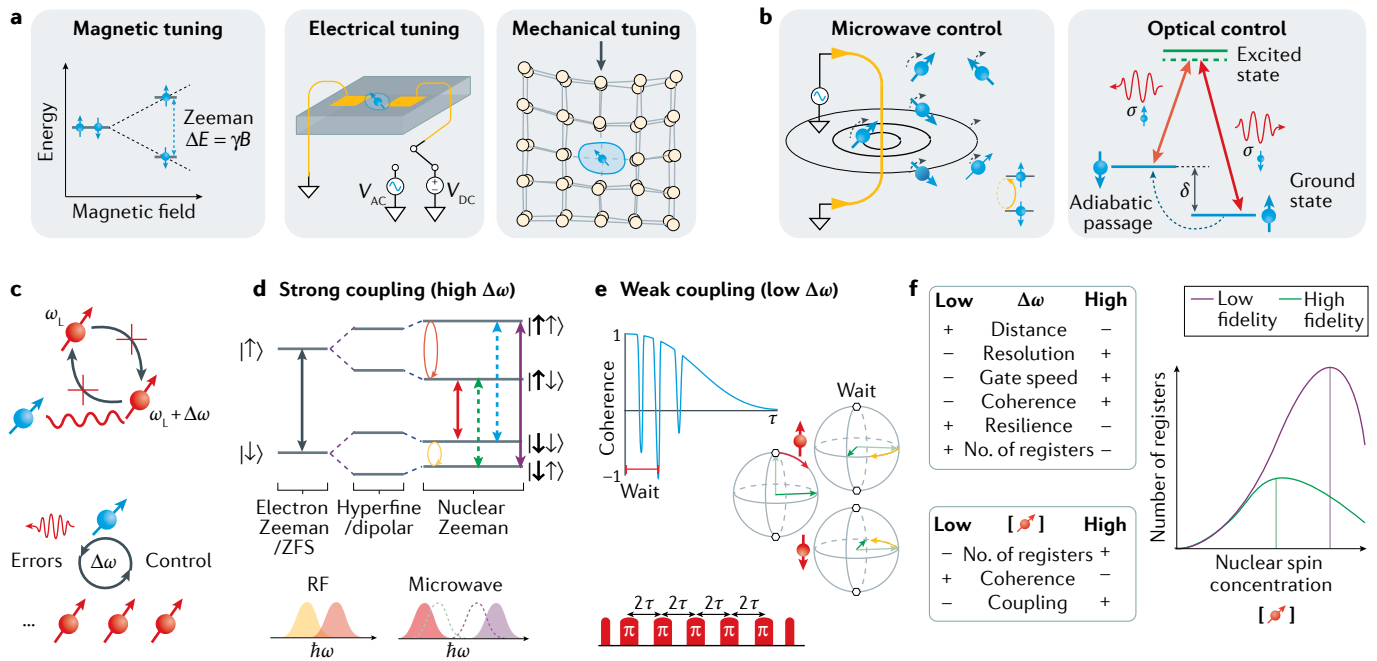
Fig. 3 | **Electron and nuclear spin control. a** | Electron spin frequency tuning via external magnetic, electrical and mechanical fields. **b** | Electron spin driving using magnetic (or other) fields at microwave frequencies (left). Optical control via an orbital excited state (right). σ indicates the circular polarization of light and δ is the ground-state spin transition frequency. **c** | Electron spin coupling to nearby nuclear spin registers in the environment. The detuning $\Delta\omega$ of the coupled nuclear spin from the rest of the nuclear spin bath is a key parameter that reduces interactions with the bath, and also sets control mechanisms and accumulated errors on the nuclear register. ω_L is the nuclear Larmor precession frequency. **d** | Nuclear spin driving schemes using resolved conditional rotations for strongly coupled spins (high $\Delta\omega$). The dotted lines indicate forbidden transitions. RF, radio frequency; ZFS, zero-field splitting. **e** | Ramsey and dynamical decoupling schemes for driving weakly coupled nuclear spins (low $\Delta\omega$), where nuclear spin-dependent phases are accumulated and projected. τ, lifetime. **f** | Trade-offs involved in the choice of hyperfine strength ($\Delta\omega$) and nuclear spin concentration (left) in terms of the positives and negatives (+ and −) and high and low values. The nuclear spin bath concentration must be chosen carefully for high-fidelity control and the number of nuclear spin registers (right)[77].

are the Bohr and nuclear magneton, respectively. The microscopic origin of each parameter is well known and their tensorial form can be predicted by ab initio calculations[79,90–95].

In addition to the magnetic field **B** in Eq. 4, all the interaction tensors and transition frequencies can be controlled by local electric fields (**E**) and strain (**ε**) that perturb the electronic wavefunction[96], as illustrated in FIG. 3a. However, the interaction tensors are affected by **E** and **ε** in different ways, depending on the symmetry and spin of the defect[97–99]. Electron spin resonance typically occurs at microwave (GHz) frequencies largely defined by the electron Zeeman interaction and the zero-field splitting. Practically, the spin's transition frequency should be large compared with the Rabi frequency, to prevent limitations from the rotating-wave approximation[100], yet, low enough to avoid microwave losses and instrumentation difficulties. Magnetic fields provide the simplest coherent spin control of $\Delta m_s = \pm 1$ transitions using microwave striplines and resonators (FIG. 3b), though it is challenging to independently manipulate nearby spins. This may be solved using magnetic field gradients[5] or local detuning through electric fields[101] or strain[102], for example.

Alternatively, nearby spins can be selectively addressed and driven with electric fields confined in nanodevices.

Electric field modulation of the zero-field tensor results in $\Delta m_s = \pm 2$ transitions[103], whereas electric field modulation of the hyperfine interaction results in $\Delta m_s + \Delta m_I = 0$ (flip-flop) transitions[71]. Recent demonstrations have also shown electric driving of the quadrupolar interaction for nuclear spins in Sb dopants in silicon[104].

Mechanical (phonon) control of the spin state works by creating local crystallographic strains (FIG. 3a), for example, in a cantilever or acoustic resonator, which allow for full ground state control of both the $\Delta m_s = \pm 1$ and $\Delta m_s = \pm 2$ transitions[97,105]. Typically, the spin–strain coupling is small. Nonetheless, a strong coupling is desired for quantum transduction between spins and phonons[106], at the potential trade-off of reduced T_1.

For a given two-level system, the longitudinal component of the interaction dipole provides tuning of the spin frequency, though at the expense of sensitivity to noise. Coherent qubit control is commonly achieved by resonantly driving the transverse components of the interaction. For example, this makes defects with anisotropic g-factors such that $g_{zz} \ll g_{xx,yy}$ interesting for balancing fast driving speeds with low decoherence, but at the cost of reduced frequency tuning. Ideally, a spin should be insensitive to fields that are prominent and uncontrolled (noise), but sensitive to fields that are generated for control or for sensing. In addition, achieving

high-fidelity control can prove challenging, owing to decoherence processes and inhomogeneous effects induced by the local environment. Techniques such as optimal control[107], adiabatic passage[108] or composite pulses[109] aid in mitigating these effects.

Ground state electron spin manipulation is also available by optical excitation, which utilizes the orbital excited-state levels as an intermediary, for example in Λ-like and V-like systems (FIG. 3b). This enables the use of optical techniques developed in the context of trapped ions and cold atoms[110], including coherent population trapping (CPT) and electromagnetically induced transparency (EIT)[111,112]. These methods are based on coherent dark dressed states, allowing for optical initialization, manipulation and readout[113–115]. Furthermore, two-qubit gates between two defects' electron spins can be mediated by light in a photonic cavity[116].

For optical control, excited-state effects (such as the optical lifetime, coherence and spectral hopping) are all major sources of errors that limit control fidelities[117]. Many methods have been developed to mitigate these issues, including stimulated Raman adiabatic passage (STIRAP), geometric phase and holonomic control[113,117,118] and superadiabatic approaches[119]. Optical control offers localized spin driving limited by the optical spot size of the excitation laser, and sub-diffraction control when combined with spectral resolution[120,121].

In summary, understanding the spin Hamiltonian and defect–host coupling is critical towards achieving high-fidelity coherent control. This control originates from the ability to tune and modulate components of the spin Hamiltonian via magnetic fields, electric fields and strain. The guiding trade-off is the balance of controlled interactions with uncontrolled noise that causes decoherence. The use of optical transitions and excited-state orbitals provides an alternative pathway for such control. Specific applications require distinct defect and host properties (such as symmetry, g-factor, piezoelectricity and so on).

Nuclear spin registers. Besides being a source of decoherence for the defect's electronic spin, nuclear spins can act as key components for quantum communications[27,122,123], computation[124,125] and sensing[126]. Owing to the low magnetic moment of nuclear spins and their weak interactions with the lattice, these states can have extremely long spin coherences[12,55,127] and lifetimes[128]. There are two major types of nuclear spins: intrinsic nuclear spins within a defect containing impurity atoms and extrinsic nuclear spins in the atoms surrounding the electronic defect, mainly the non-zero nuclear spin isotopes of the host crystal.

For intrinsic systems, every defect can deterministically have one or more corresponding nuclear spin registers with the proper choice of isotope during defect formation[129–131]. The hyperfine interaction for intrinsic nuclear spins can be large from the contact term (up to GHz (REF.[132])). This usually results in a strongly coupled electron–nuclear spin system with nuclear spin-resolved transitions, depending on the electron spin linewidth, $\Gamma = 1/(\pi T_2^\star)$. Importantly, the host crystal can be fully isotopically purified while still retaining this intrinsic register[77,78].

However, to extend beyond one nuclear spin for each defect, extrinsic nuclei are necessary. They are also the only nuclear spins available for vacancy-related defects, which do not contain an impurity atom. Extrinsic defects can produce a few strongly coupled nuclear spins for the first few neighbouring sites in the lattice, depending on Γ.

There are two broad choices for nuclear spin control: direct resonant driving or conditional phase accumulation, depending on the frequency shift $\Delta\omega$ imparted by the hyperfine interaction with the electron spin (FIG. 3c). With the presence of this control, nuclear spin initialization by single-shot measurement[55] or by swapping polarization with the electron are possible[125]. In strongly coupled electron–nuclear spin systems, $\Delta\omega$ is large compared with Γ and the nuclear spin states are sufficiently resolved for direct magnetic driving of fully entangling two-qubit gates[124], consisting of electron–nuclear conditional rotations, as shown in FIG. 3d. Spin selectivity here requires significant nuclear Zeeman interaction (high magnetic field), a quadrupole interaction or hyperfine differences between spin sublevels.

The second way to mediate two-qubit gates is by creating an electron spin superposition and accumulating a nuclear spin-dependent phase[55] (FIG. 3e). The spin state selectivity is similarly limited by the spin's $T_2^\star$ and requires a hyperfine interaction that is faster than the dephasing time. Extending the number of registers to include weakly coupled nuclear spins with small frequency shifts $\Delta\omega$ can be achieved with dynamical decoupling-based control. This extends the $T_2^\star$ limit to T_2 by cancelling all interactions with the environment but those at a frequency set by the inter-pulse spacing of the decoupling scheme (FIG. 3e). When this frequency matches that of a nuclear spin transition, the electron spin accumulates a nuclear spin-dependent phase, depending on the quasi-unique signature from $\Delta\omega$, selective down to single nuclei in the lattice[133,134]. This technique (and variants with interleaved radio frequency tones[12,135]) allows both controlled and uncontrolled rotations on the nuclear spin[12].

Both schemes result in gate speeds ranging from a few microseconds to a few milliseconds. They have allowed for the control and entanglement of more than ten nuclear spin registers[12,135], as well as proof-of-principle error correction[124,125] for quantum computing and communications, along with QND readout enhancement[126] and the ability to resolve single nuclei at a few nanometres distance[136] for quantum sensing. Overall, the total experimental sequence length sets the frequency resolution (from the Fourier transform) of the control and is ultimately limited only by the spin's T_1, leading to a trade-off between the number of resolvable registers and the total gate time[77]. For weak hyperfine interactions, the number of possible nuclear spins grows greatly as the allowed gate time is increased, defined by the large ratio of T_1 to $T_2^\star$.

The interplay between the hyperfine interaction strength and the isotopic abundance is critical[77] (FIG. 3f). A strong hyperfine interaction allows for fast gate times and long coherence times as flip-flops between nuclear spins can be suppressed by the hyperfine-induced detuning $\Delta\omega$ (known as a 'frozen core')[137]. Controlling a nuclear spin species that has a different gyromagnetic

ratio than the bath spins also avoids this channel of decoherence at high magnetic fields. Isotopic purification increases both the electron and the nuclear spin coherence times, yet, reduces the availability of nuclear spins that can be used. Conversely, at high nuclear spin concentrations, the ability to resolve nuclear spin transitions is limited by spectral crowding[77,124], which reduces the two-qubit gate fidelities.

Similar to T_1 relaxation, protocols that involve optical excitation of a defect can randomize the electron spin state or hyperfine interaction during illumination, and, therefore, modulate the nuclear spin frequency and reduce its coherence[55,122,138]. Generally, the robustness of the nuclear spin can be described by the decay of the state fidelity F:

$$F = \frac{1}{2} + \frac{1}{2^{N+1}}\left(1 + e^{-\frac{1}{2}(\tau\Delta\omega)^2}\right)^N \qquad (5)$$

where τ is the timescale of the uncontrolled dynamics and N is the number of uncontrolled events[122,138,139]. The fidelity exponentially improves by reducing $\Delta\omega$. This makes nuclear spins with low hyperfine interactions (~kHz) desirable for nuclear-assisted QND readout or quantum communication[122], where many optical cycles or gates on the electron are required. Electrical readout schemes that rely on ionizing defects can similarly dephase nearby nuclear spins through modulation of the hyperfine interaction[140].

Overall, the impurity atoms present in a defect complex and the atoms in the lattice determine the availability and performance of nuclear spins to manipulate. From an engineering perspective, delta-doping nuclear layers[79], heteronuclear crystal hosts[64] and isotopic engineering[77,141] are promising tools.

In summary, nuclear spins are vital components for solid-state quantum technologies. Nuclei intrinsic to the defect can be easily leveraged to boost quantum sensing, whereas extrinsic nuclear spins provide multi-qubit registers and long-lived quantum memories for sensing and communications. In utilizing these spins in the solid state, a careful choice of isotopic concentration is needed to balance spectral crowding, coherence and nuclear control. Guidelines for quantum applications with nuclear spins include a need for resiliency to enable control on the defect's electron spin, single-shot readout capability and long coherence times.

Conclusions. Electron and nuclear spins display some of the most compelling properties for solid-state defect qubits. Important considerations relate to the host material, including isotopic purity, defect concentration and material properties (such as piezoelectricity and Debye temperature). The details of the ground (and sometimes excited) state spin Hamiltonian define the possible control and decoherence mechanisms. Their incredibly long spin lifetimes and coherence times have shown that these systems are robust quantum memories. Continuous progress towards higher-fidelity control of large nuclear spin clusters[12] can lead to small, noisy quantum computers or single, high-quality logical qubits from error-correcting the clusters.

Optical properties

The optical addressability of many spin defects provides a photonic interface for quantum applications, driving materials research for defects with optimal optical properties. Though electrical (see the section on the spin–charge interface) and other methods[56] exist to initialize and read out the spin state, an optical interface is generally desired for its practical ease of use and for the possibility of isolating single defects. An efficient interface requires understanding the major optical parameters of a spin defect, including the emission spectrum, quantum efficiency and spin-dependent optical contrast.

Optical emission and excitation. The emission wavelength is a basic property that influences factors such as the attenuation through various media and the required detector technology. For quantum communication, infrared photons are preferred to reduce optical fibre losses (FIG. 4a). This has driven interest in defects that emit in the telecom band, including erbium (1,536–1,550 nm)[142] and vanadium dopants (1,280–1,390 nm)[45,143]. Likewise, applications in biosensing are optimized around 1,000 nm in the 'second biological optical window' dictated by low photon absorption in saltwater[144]. For integrated, low-cost applications, silicon detectors operate optimally at 400–1,000 nm, whereas high quantum efficiency can be achieved with superconducting nanowires in the infrared, at a higher cost.

A desirable emission wavelength can be engineered by sum and difference frequency conversion using nonlinear optical phenomena such as spontaneous parametric down-conversion (SPDC) and spontaneous four-wave mixing (SPWM), often in a periodically poled material[145]. When mixing single photons, however, Raman scattering and other sources of scattering can produce noise in the output band of interest, depending on the chosen input pump wavelengths[146]. Importantly, these techniques can preserve the phase coherence of the input photons, which is required for entanglement protocols[145,147].

The photon emission rate is a critical aspect of optically active defects because it defines the experimental signal intensity, the photon count rate of single-photon sources, the sensitivity of the defect as a quantum sensor and the entangling rate for quantum communication. The photon count rate is dictated by the radiative rate from the excited state, but is reduced by non-radiative rates and experimental collection efficiencies, typically <1% in confocal microscopes[148] (FIG. 4b).

Efficient collection can be addressed via solid immersion lenses and surface metalenses that reduce the effect of total internal reflections, and even collimate the emitted light, leaving the sample for efficient free-space collection[148,149]. Alternatively, photonic waveguides can enable direct fibre coupling of the light[8,150,151]. The photon generation rates can be enhanced by using small-mode-volume, low-loss cavity structures with a high Purcell factor to reduce the excited state lifetime. Practically, photonic structures can be fabricated directly into the material[8,151–153], deposited on top[150] or made through flip-chip device integration[142].
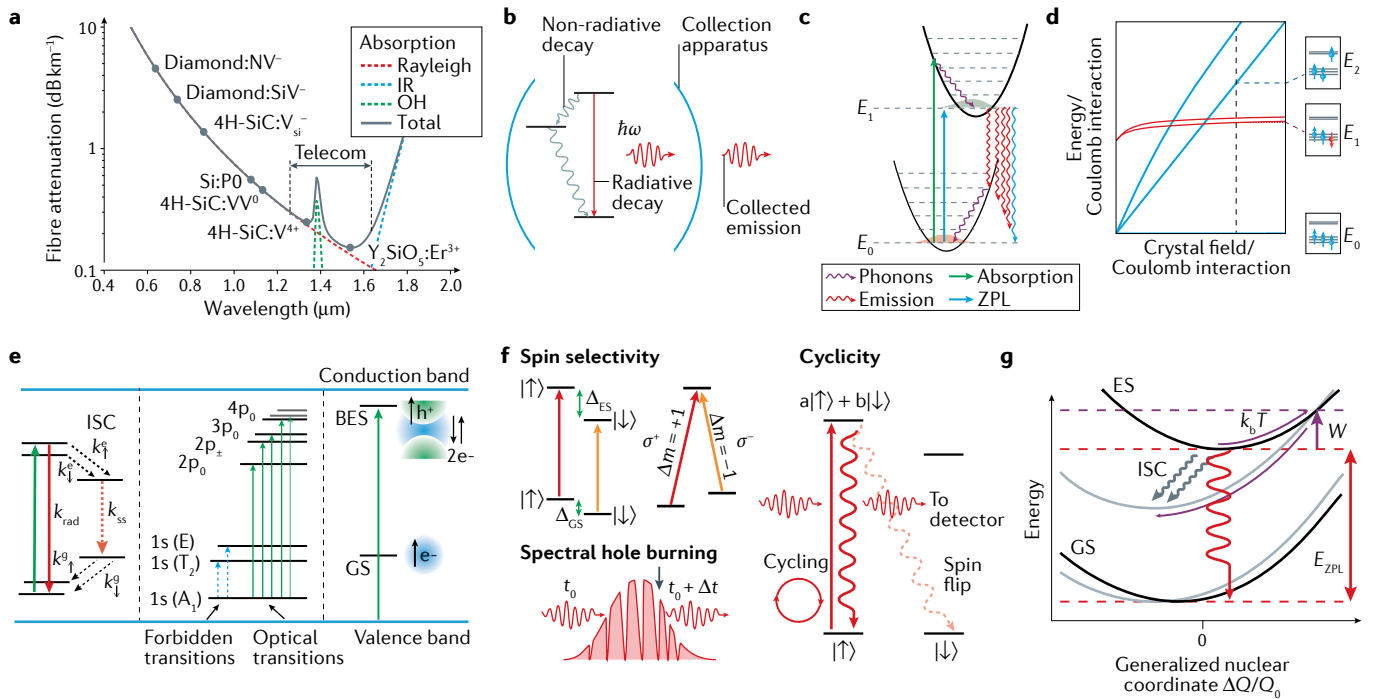
Fig. 4 | Optical properties of spin defects in the solid state. **a** | Attenuation loss as a function of wavelength in an optical fibre[268]. Typical defect emission wavelengths are shown to compare their viability for quantum communication (without frequency conversion). IR, infrared; OH, hydroxyl ions. **b** | Radiative and non-radiative emission of a defect in a collection system, such as free-space optics or photonic cavities. **c** | Phonon-assisted and zero-phonon line (ZPL) absorption and emission from defect orbitals, showing the harmonic vibration potentials in a Franck–Condon diagram. E_0, lowest ground-state energy; E_1, lowest excited-state energy. **d** | Tanabe–Sugano diagrams for predicting orbital structures in transition metal ions. Shown here is a d^3 orbital with octahedral coordination (such as that of Cr^{3+}:MgO), with corresponding energy-level and spin assignments for the t_{2g} and e_g states on the right. **e** | Common electronic orbital-level ordering for defects: from left to right, intersystem crossing (ISC) for spin polarization and readout, the many hydrogen-like excited states of a dopant (for example, in silicon), ground state (GS) and associated bound-exciton state (BES) of a donor or acceptor. For the sake of simplicity, the labels valence band and conduction band in the manuscript are used, respectively, for hole and electron ionization thresholds,

with which they normally only coincide for single-particle levels. k^e, k^g, k_{rad} and k_{ss} are the excited state-to-ISC, ISC-to-ground state, radiative and ISC decay rates, respectively. **f** | Spin-selective optical transitions can occur as spin-resolved optical transitions from frequency detuning (left) or as a non-conserving spin transition using polarization selection rules (right). Spectral hole burning in ensembles is used for controlled single-photon storage. Cyclicity is defined by the spin mixing in the excited state, which causes spin-flip transitions. The red wavy arrows represent the absorption and emission of photons. Δ_{ES}, excited-state spin transition frequency; Δ_{GS}, ground-state spin transition frequency; $\sigma^{+/-}$, circular polarization of light; m, spin projection. **g** | Non-radiative effects from phonon relaxation and their influence on spin-dependent optical processes that can exist in some defects with an intersystem crossing (ISC, grey arrows). The triplet (black) and singlet (grey) potential energy surfaces are shown with respect to normalized displacements along a harmonic vibrational mode ($\Delta Q/Q_0$). Nonselective transitions (purple) can proceed with characteristic energy W. Panel **g** is adapted from REF.[201], CC BY 4.0 (https://creativecommons.org/licenses/by/4.0/).

The emitted photons are spectrally divided into a narrow zero-phonon line (ZPL) and a broad phonon sideband (PSB) (FIG. 4c). The observed emission and absorption spectra are typically interpreted using a Huang–Rhys model (with predictable factors)[154,155] that provides information about the vibrational structure of the defect's luminescence band[156]. The Debye–Waller factor (DWF) is the key quantity that describes the ratio between the ZPL emission intensity and the overall emission intensity. A low DWF is often due to a strong phonon coupling, resulting in decay between the excited state and the higher phonon modes of the ground state[157]. Applications that require photon coherence or interference benefit from a dominant narrow ZPL spectral contribution (high DWF) that contains indistinguishable photons. Nanophotonic cavities provide an engineering pathway for increasing the ZPL emission and the DWF[158,159].

The quantum efficiency (QE) is another key parameter for assessing the performance of an optical emitter.

QE is the fraction of excitation events that result in the emission of a photon, and is lowered by non-radiative and ionization rates. The QE can be obtained indirectly by comparing the measured optical lifetime to the radiative rates calculated with density functional theory (DFT[160]) or by combining master equation modelling and experimental spin-dependent transient decays[161]. Direct experimental measurement of the QE can be achieved by controllably varying the photonic density of states[162]. Similarly, Purcell enhancement can improve the QE by changing the balance between the radiative and non-radiative rates.

The radiative and non-radiative decay routes depend on selection rules such as conservation of total spin S, the symmetry of the defect and the strength of the optical transition dipole moment, spin–orbit coupling and electron–phonon coupling[163]. The orbitals for defect complexes are generally not known, except for simple cases such as those described by the effective mass theory

(for example, donors in silicon)[164]. From the highest symmetry set by the host crystal[26], the defect point group symmetry can be lowered for defect complexes with static Jahn–Teller distortions or with strain. With significant spin–orbit interactions for which the total angular momentum J becomes the relevant quantum number, normally 'forbidden' transitions become weakly allowed with long optical lifetimes[165]. Other considerations include the case of centrosymmetric defects in which transitions are allowed when the starting and ending molecular orbitals have opposite parity, for example[166].

Single-particle orbitals and levels for particular defects in a host crystal can be computed by DFT or higher levels of theory (such as GW[167]). Molecular orbitals are constructed from these single-particle orbitals according to the number of electrons and holes, Jahn–Taller distortions, Hund's and Pauli's rules, and the degeneracy of the orbitals (and labelled according to the overall symmetry and spin multiplicity). The single-particle orbital degeneracy directly sets the possible spin multiplicities. $S > 1/2$ systems require (nearly) degenerate single-particle orbitals, for example. The filling and ordering of single-particle orbitals at a given charge state can be obtained by DFT and post-DFT calculations (such as quantum embedding theory[160,168]) to construct the defect's molecular orbitals.

Depending on the defect, the optical properties may or may not be affected by the material host. To one extreme, the intra-f-shell transitions in rare-earth ions are largely decoupled from their site location and the details of the host lattice, and, therefore, are transportable across multiple materials. The optical properties of transition metal defects are similarly confined to the d-orbitals of the ion[45,165,169]. However, these orbitals are sensitive to the coordination, symmetry and crystal field strength that the ion experiences. If two hosts share similar properties (for example, symmetry), then the resulting d-orbital physics is translatable across platforms[165] and can be understood directly through Tanabe–Sugano diagrams[170,171] (FIG. 4d). For vacancy-related defects, the details of the resulting dangling bonds and their interaction and relaxation within the lattice define the major optical properties of the defect. Finally, the hydrogenic states of bound excitons are largely determined by the position of their energy levels in relation to the bandgap, not by the details of the internal defect structure, and simplified selection rules from atomic physics can be used[164] (FIG. 4e).

In summary, optical emission properties play a significant role in the practical implementation of defects. These guidelines include the need for telecommunication wavelengths for low-loss fibre transmission for quantum communication, and high DBF and QE for bright optical emission. Optical devices, such as nanophotonic devices, can be used to increase collection efficiency and photon count rates. Finally, the defect symmetry plays a critical role in determining the spin and optical structures of defects.

Spin–photon interface. The spin-dependent optical processes of defects are essential features for spin-based quantum information. Without them, light could not be used to polarize, control or read out spins. There are two main ways that the spin of a defect can influence the coupling to light: optical transitions with spectrally or polarization-resolved spin states or via an intersystem crossing (ISC) with spin-dependent non-radiative processes. Both of these processes unlock optically detected magnetic resonance (ODMR) of the spin state of the defect.

In the first case, optical polarization (linear or circular) can lead to different optical selection rules depending on the spin state[172], and, hence, to spin-dependent excitation and emission of photons. Alternatively, spin selectivity is obtained when two or more spin states in the ground state have different optical transition frequencies to one or more spin states in the excited state[27] (FIG. 4f). This frequency resolution requires that the optical linewidth be narrower than the spin-dependent optical shift.

Spin-dependent frequency differences between orbital ground and excited states can arise from different electronic wavefunctions and corresponding spin interactions. This includes differences in the g-factor (such as in Si vacancies in diamond[173] and Er-based systems[69]), hyperfine or zero-field tensors (for $S > 1/2$, such as the NV centre in diamond[19] or vacancy centres in SiC (REFS[161,174])). A total spin change in the excited state, as with some transition metal systems[175], results in a controllable Λ-system with spin-selective transitions.

For many applications, the spin eigenstates must remain identical between ground and excited states, otherwise the defect would suffer from non-spin-conserving radiative decay from the excited state (FIG. 4f). A low spin-flip probability is desired to create so-called 'cycling' transitions, in which, upon excitation and emission of a photon, the defect is returned to its initial spin state[27]. With this, photons can be continuously extracted from the defect with high correlation to the spin state, which is critical to the fidelity and verification of spin–photon entanglement for quantum communication protocols[121,172].

Unfortunately, many of the mechanisms that provide spin-selective optical transitions can also contribute to mixing of the spin eigenstates. For example, in some diamond and SiC defects, the axial spin–orbit term λ_z creates the frequency splitting needed for spin–photon entanglement, whereas the transverse spin–orbit mixing $\lambda_\perp$ degrades the spin selectivity of the transitions and reduces the cyclicity[19]. Additionally, mixing of the spin eigenstates can be reduced/increased by controlled/uncontrolled magnetic fields, electric fields and strain[159,176,177], and Purcell enhancement can increase the cyclicity by changing the balance between different radiative rates[158].

Conversely, non-spin-conserving transitions are required to optically polarize and control the spin ground state. Related to optical pumping in atomic physics, pumping on a transition eventually results in a spin flip, due to finite cyclicity, and, thus, in the selective depletion of one spin state[70,175]. This optical process results in a high degree of spin polarization beyond the thermal Boltzmann distribution, enabling spin operation at room temperature and above, provided the spin's T_1 is long compared with the spin-flip rate.

In ensembles, even if the spin-selective structure is inhomogeneously broadened and unresolved, optically pumping the population from a specific spectral band can create spin polarization. These 'spectral holes' can be recovered by microwave excitation or by optical means, probing the internal structure within the broadened ensemble[178]. The characteristic time by which the hole recovers is a measure of the spin's T_1 (REFS[45,70,175]). For rare-earth systems, creation of a 'comb' of spectral holes allows the ensemble to act as a controllable quantum memory for single photons[179] (FIG. 4f).

Without spin-selective optical excitations, the alternative pathway for optical spin readout and polarization is via spin-dependent non-radiative processes such as ISCs. ISCs are non-radiative transitions between orbital levels with different spin multiplicity but the same symmetry, and they are mediated through phonons and the spin–orbit interaction (λ)[180]. Because vibronic mixing and Jahn–Teller distortions in the excited states can mix the different orbitals, resulting in different symmetries, the associated spin projections can couple differently to the ISC through the spin–orbit interaction[181]. Multiple states may be desired in the ISC decay channel to closely match the energies of the ground and excited states for appreciable ISC rates. In general, the ISC rate goes as $\lambda^2 F(E)$, as described by the Franck–Condon theory, where F is the phonon overlap spectral function at the energy spacing E between the levels mediating the ISC[182]. Phonons drive the configurational change of the atoms in the defect for the ISC, whose exact potential energy surfaces (PESs) determine the dynamics. For systems with strong electron–phonon coupling, extensions to vibronic states analogous to the Herzberg–Teller theory of the optical spectrum[181,183] can also determine the weakly allowed optical transitions within the ISC. The exact mechanisms for the ISCs for various defects are a subject of extensive theoretical and experimental work[160,161,182–184].

The addition of spin-dependent non-radiative rates, as well as intermediate orbital 'shelving' states in the ISC, results in spin-dependent emission probability of a photon during the optical cycle (FIG. 4c). This core feature allows for ODMR, in which the spin–photon interface may be unresolved, such as in room-temperature and quantum sensing applications.

The spin dependence of non-radiative processes depends on the temperature of the system. For the ISC, the PES of the states for each spin multiplicity can be calculated as a function of the nuclear coordinates of the defect. If an energy barrier (W) exists between PESs with different multiplicity, then direct transitions between these PESs at their crossing point are unlikely[185]. Thermal crossing of the barrier, however, can destroy the spin dependence of the non-radiative ISC rates, while also reducing the QE[185] (FIG. 4g). The ability to calculate W is, thus, crucial to designing room-temperature qubits. Thermal activation through this process modifies the radiative lifetime τ as a function of temperature T as follows[185]:

$$\tau(T) = \frac{\tau_0}{1 + s \cdot e^{-\frac{W}{k_b T}}} \qquad (6)$$

where τ_0 is the optical lifetime at zero temperature and s is the ratio of non-radiative to radiative rates at the PES crossing point. Spin polarization and measurement contrast using the ISC depends on the relative rates and lifetimes of the system[186], and, by knowing all these rates, the optical illumination and readout durations can be optimized for the highest ground-state spin polarization (up to 96%[161]), contrast (up to 30%[186]) and number of extracted spin-correlated photons (relating to the signal-to-noise ratio). Finally, it is important to note that the properties yielding a desired ISC often conflict with an ideal radiative and spin-conserving spin–photon interface. Additionally, the mixing from the presence of an ISC, by definition, reduces the state purity of the defect's spin.

In summary, an ideal spin–photon interface requires a mechanism that maps the qubit spin state to a property (polarization, time, energy) of light constituting spin–photon entanglement. Both cycling and non-cycling transitions are desired for single-shot readout and efficient spin polarization within the spin relaxation time. These properties are key for quantum communications. Guidelines for systems with an ISC include singlet states close in energy to the ground and excited states, high spin selectivity between the ISC rates into or out of the ISC and a large energy barrier (W) that unlocks elevated-temperature operation for quantum sensing.

Optical coherence. Aside from ground-state spin coherence, the coherence of the orbital transitions has important consequences for quantum technologies. Reduced optical coherence can be detrimental to resonant readout protocols[177], spin initialization, optical spin control[117] and signal-to-noise ratio for quantum sensing[187]. Critically, the coherence of an emitted photon directly influences the fidelity and entanglement rate of quantum communication protocols[188,189]. These considerations result in certain applications choosing optimal optical performance over better spin properties[8].

For optical transitions, the relevant coherence for single emitters is usually the optical T_2^* or, inversely, the optical linewidth Γ. An optical emitter with a lifetime τ has a best-case 'lifetime-limited' or transform-limited homogeneous linewidth (full width at half maximum, FIG. 5a) of:

$$\Gamma_0 = \frac{1}{2\pi\tau} \qquad (7)$$

This optical linewidth reflects the coherence of the emitted light from the defect, which can also be measured directly through the decay of optical Rabi oscillations[190] (FIG. 5b). Additional non-radiative processes can shorten optical lifetimes and, therefore, increase Γ (FIG. 5c).

With two perfectly indistinguishable emitters, coherent interference between two emitted photons on a beam splitter erases the path information of the photons and causes a Hong–Ou–Mandel interference dip[191] (FIG. 5d), enabling heralded entanglement[192]. This photon-mediated interaction is the key mechanism by which spin defects can produce and distribute
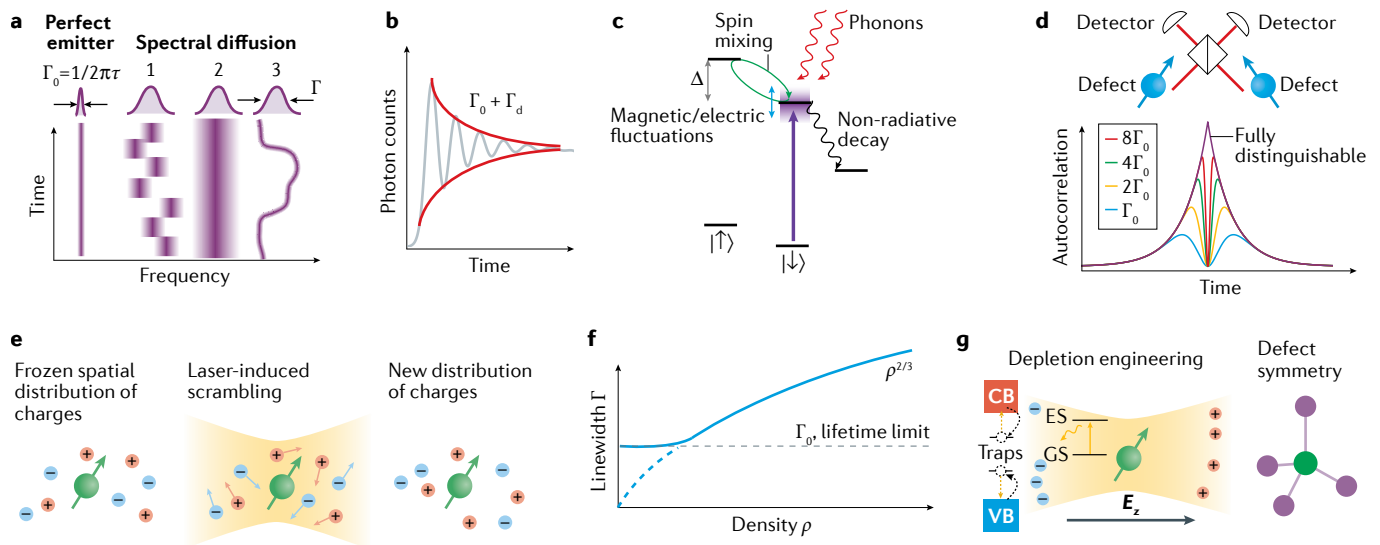
Fig. 5 | **Considerations for optical coherence. a** | Various types of spectral diffusion depending on the noise correlation time: (1) discrete spectral jumps, (2) Gaussian broadened line ($\tau_c < \tau$) and (3) spectral wandering. Γ_0 is the full width at half maximum optical linewidth and τ the lifetime. **b** | Decay of optical Rabi oscillations through time-resolved fluorescence. Γ_d is an additional decoherence contribution. **c** | Possible mechanisms for orbital decoherence and decay. **d** | Hong–Ou–Mandel interference between emitted photons from two defects at a beam splitter. A correlation dip is formed for indistinguishable emitters and is degraded with increased linewidth Γ. **e** | Mechanism for spectral diffusion through photoionization of charge traps. **f** | Linewidth dependence on charge trap density ρ, with the scaling $\rho^{2/3}$ and the lifetime limit Γ_0 indicated[202]. **g** | Possible strategies for mitigating spectral diffusion: depletion of the fluctuating charges (left) or engineered defect symmetry for reduced Stark dipole (right). CB, conduction band; ES, excited state; E_z, electric field applied in the z direction; GS, ground state; VB, valence band. Panels **d** and **e** are adapted from REF.[201], CC BY 4.0 (https://creativecommons.org/licenses/by/4.0/). Panel **g** is adapted with permission from REF.[198], AAAS.

entanglement at long distances. With imperfect emitters, the reduced phase coherence of the photons reduces the interference visibility and the integration window over which events can be collected[189]. This drastically decreases the entanglement rates and fidelities achievable with defect spins.

A defect's orbital structure can undergo multiple types of broadening, depending on the correlation time of the noise (τ_c) and the noise source. Broadening can manifest differently depending on the experimental timescale τ as either a Gaussian broadened line ($\tau_c < \tau$), discrete spectral jumps from experiment to experiment ($\tau_c \sim \tau$) or a 'spectral wandering' ($\tau_c > \tau$, FIG. 5a). Phonon-induced optical decoherence occurs through similar processes, as discussed in the section on spin lifetime, with direct, Raman and Orbach processes with characteristic temperature scaling[193,194]. In this case, the temperature power law varies between degenerate and non-degenerate orbitals (instead of between Kramers and non-Kramers spin systems) and is dependent on any orbital splitting Δ. Similar to the spin T_1, a small spin–orbit coupling and large Debye temperature are desired to maintain a lifetime-limited optical line at the desired temperature.

Spectral diffusion refers to broadening from environmental noise that is slow compared with the optical lifetime, whereas pure dephasing occurs from noise that is fast compared with the emitter's lifetime. For example, thermal drift during the experiment can manifest as slow spectral wandering[193]. Magnetic field fluctuations can broaden and dephase the optical transition, for example, in systems with spin–photon interfaces

based on a g-factor difference[195] (FIG. 5c). Isotopic purification may not only narrow ensemble linewidths due to mass shifts[196] but also narrow magnetically sensitive lines[69,197]. Generally, electrical noise tends to be the dominant source of spectral diffusion and broadening for defect energy levels. If a defect does not have inversion symmetry, it has a non-zero, first-order Stark shift dipole that shifts the energy levels under applied electric fields, usually of a different amount for the ground and excited levels[174] (see the section on optical emission and excitation). Electric field fluctuations are often caused by surface defects[51], through photoionization of nearby impurities[198–200] or by tunnelling to a nearby charge reservoir (FIG. 5e). For charge noise from impurities in semiconductors, the total broadening from spectral diffusion can be understood from both theoretical treatments and Monte Carlo simulations of charge noise[201,202], in which even high-quality semiconductor crystals with part-per-billion density (ρ) of impurities and traps cause significant broadening ($\Gamma \propto \rho^{2/3}$, FIG. 5f). This imposes strict criteria on the purity and quality of the host crystal after growth and defect formation.

Most optical transitions of a defect are tunable[200] and dephased by electric fields[198]. Defects with inversion symmetry or exhibiting the same shift in the ground and excited states levels[174] can display near-transform-limited optical lines, even in nanostructures, and can still be tuned with strain fields[44]. Strain tuning should not break the inversion symmetry, otherwise, the protection is degraded, and sensitivity to strain must not be so large as to cause additional broadening mechanisms. An important metric is, therefore, the ratio of the optical

frequency tuning range to the static inhomogeneous optical linewidth (for example, caused by different local strain or electric fields). For long-distance entanglement where photons need to be indistinguishable[15,203], the achievable tuning range of a defect should be larger than the distribution of optical frequencies. For example, tuning over this range should be possible before reaching dielectric breakdown or mechanical failure.

Besides growing high-purity materials, the fluctuating charges can be depleted turning an electrically noisy environment into a clean one while maintaining Stark sensitivity[198] (FIG. 5g). Fast frequency tuning of the optical lines can allow feedback techniques to stabilize and reduce the linewidth[204]. By contrast, large Purcell factor enhancements may be beneficial by causing an increased homogeneous linewidth that overwhelms the environmental noise without limiting interference visibility.

In summary, systems with high Debye temperature, low spin–orbit coupling and high symmetry are desirable for optimal optical coherence properties. Optical coherence is the key parameter that determines the rate and fidelity of photon-mediated entanglement for quantum communications. Other guidelines include the need for transform-limited linewidths and low orbital decoherence at a desired temperature, while maintaining a degree of tunability for the spin–photon interface. For the host material, this can be achieved through low impurity concentrations, depleted charge environments or engineered defect symmetries.

Conclusions. The optical properties of spin-qubit systems offer a natural spin–photon interface to initialize, manipulate and read out the spin state, as well as to mediate entanglement through photons. Important considerations must be made as to the emission wavelength, spectral line shape and spin contrast when selecting the most appropriate defect for a given quantum application. This choice needs to balance transform-limited linewidths, emission brightness, spectral diffusion and other physical mechanisms that affect the radiative and non-radiative emission rates. Optical engineering can improve these emission properties, but requires tackling the complexity of integrating spin defects into photonic devices.

Charge properties

The charge properties of spin defects in the solid state are fundamental to their reliable use, as well as for electrical readout of the spin state. Studying these properties was instrumental to the development of classical condensed matter and semiconductor physics. However, the focus in quantum science is on specific defects and how they can be used, and not on the overall transport properties, as is often the case for classical electronics. Hence, a new set of characterization tools and understanding is required.

Charge state. All well-known spin defects correspond to specific charge states (for example, the negatively charged NV centre in diamond), while a different charge state leads to radically different spin and optical interfaces. It is, therefore, critical that the charge state is initialized on demand and is stable during qubit operation. The first condition ensures that a large fraction of

a defect ensemble contributes to the signal and a lower fraction contributes as a dephasing spin environment, both being important aspects for sensing applications[205]. For single spins, a known initial charge state is essential for more complex applications such as single-shot readout and deterministic entanglement[192]. The second condition prevents an additional T_1 relaxation channel from random charge state switching, while the stability of surrounding defects in the host reduces the intensity of electrical and magnetic noises that deteriorate the spin and optical coherences[198].

Predicting charge stability demands both a theoretical understanding (for example, from DFT or higher level of theory[206]) and a precise knowledge of the material quality. Electronic structure calculations provide the transition energies between two charge states from formation energy calculations[163], as illustrated in the bottom left part of FIG. 6a. The charge transition level between the charge states 0 and −, for example, is denoted (0/−). The difference in energy between this level and the conduction/valence band is the energy required to remove (− to 0)/add (0 to −) an electron from/to the defect. Using DFT calculations performed for optimized configurations of the defect, optical ionization energies may be inferred from computed charged states by including the Franck–Condon shift, with accuracy that depends on the adopted energy functional. The charge transition level for single donors or acceptors is close in energy to the ZPL emission within the binding energy of the exciton. From the electronic wavefunction, the density of states and overall electronic structure of the defect can be calculated to obtain ionization and capture cross-section rates for simulation of charge dynamics[207].

The real complexity in understanding charge stability arises when modelling an actual sample with all relevant impurities. When there is a clear dominant species providing the majority carriers, calculating a Fermi level and transport dynamics may be achievable. However, in samples with large bandgaps and low defect concentration (10^{13}–10^{15} cm^{-3}), and under illumination at low temperature (carrier freeze-out), charge stability is dictated by the steady-state balance between the desired defect and additional electronic traps. Such balance occurs via several kinetic processes (FIG. 6b), including thermal drift, diffusion, thermal and one-photon or two-photon ionization, electron or hole capture and electron–hole generation from thermal or above-bandgap excitations[208,209].

Practically, the aim is to stabilize the defect to a desired charge configuration by understanding which process occurs under what conditions. There are three main tools for this purpose: electron spin resonance combined with light excitation[210], photoluminescence under two-colour illumination[208] and electrical measurements such as deep-level transient spectroscopy (DLTS)[207]. Each tool provides a different signal that is modulated by thermal or optical ionization of the traps and correlated with temperature, annealing or sample growth. Although exact interpretation can be challenging, combining theory and these experiments can give information such as ionization mechanisms and thresholds, optimal growth conditions or defect densities[24,207,210].
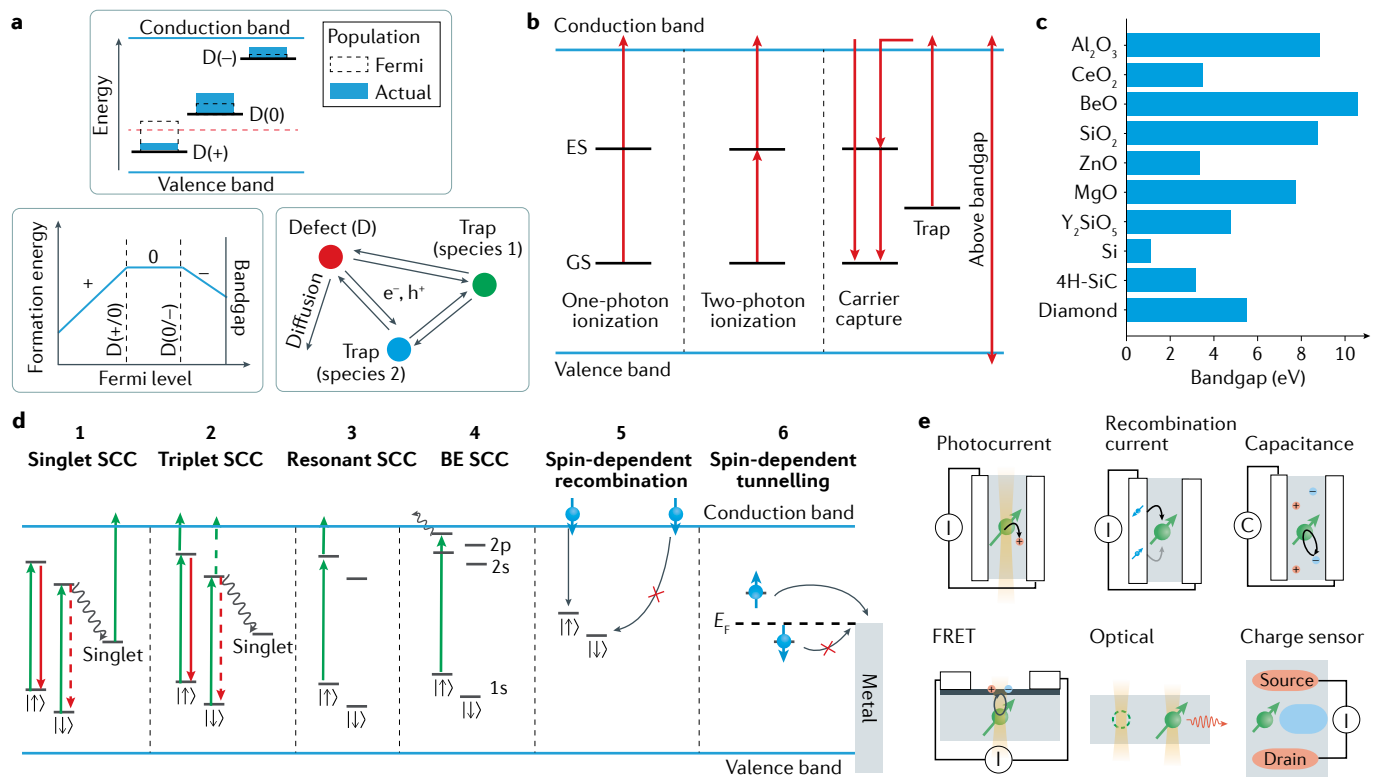
Fig. 6 | Charge state properties of solid-state defects. a | Top: population distribution of the charge state in an ensemble of defects (D). At cryogenic temperature under illumination, the population can be far from thermal equilibrium according to the Fermi level (dashed red line). Bottom left: charge transition energy levels obtained from a formation energy diagram through density functional theory calculations. Bottom right: free carrier diffusion, capture and ionization between multiple defect species. **b** | Diagram of typical processes involved in the charge dynamics of defects and free electrons. Equivalent processes are allowed with the valence band for free holes. Red arrows correspond to thermal excitation or photoexcitation. ES, excited state; GS, ground state. **c** | Bandgap of relevant host materials for quantum applications[269,270]. **d** | Multiple examples of spin-to-charge conversion (SCC): (1) spin-dependent two-photon ionization through spin-dependent shelving; (2) two-photon ionization with a spin-dependent lifetime modification; (3) two-photon ionization with spin-dependent optical transitions; (4) bound exciton (BE) SCC with either a two-photon, thermal or Auger ionization process; (5) spin-dependent capture of a free carrier to a trap; and (6) spin-dependent tunnelling. **e** | Electrical readout devices: from top left to bottom right, photocurrent readout after spin-dependent defect ionization, spin-dependent recombination, spin-dependent charge/capacitive sensing after ionization, Förster resonance energy transfer (FRET) between the defect and a secondary system[271], fluorescence readout of the presence or absence of a particular defect charge state and single-charge sensor/single-electron transistors with spin-dependent tunnelling.

Some broad considerations can be made solely with respect to the bandgap of the host material, summarized for relevant crystals in FIG. 6c. First, dopants tend to have larger binding energies with lower thermal ionization in wide-bandgap semiconductors. Second, the excited state of an optically active defect must generally be within the bandgap for photoluminescence, unless its decay rate to the band edge is much slower than its radiative rate. For a charge state q, the optical excitation energy must preferentially be between the $q+1/q$ and $q/q-1$ charge transition energies (with respect to appropriate band edges), and then optimally below a third of the bandgap to avoid two-photon ionization threshold via the excited state, either to the valence or to the conduction band. Finally, an excitation energy below half of the bandgap is also desirable to avoid mid-gap defects undergoing constant charge cycles via one-photon ionization to and from the valence and conduction bands. These considerations are valid both for the stability of the measured defect and to prevent surrounding impurities from becoming a source of fluctuating noise[198]. A bandgap above 1.6–2.4 eV is, therefore, optimal for telecom emitters, and one above 4–6 eV for visible (~600-nm) emitters, for example.

Charge stabilization can be achieved through laser control. If the laser wavelength that excites the optical transition can simultaneously repump to the correct charge state, the defect may be stabilized[200,208]. Multi-colour excitations can help create the correct balance of ionization rates for all local traps[208,211]. In addition to optical manipulation, electrical techniques such as depletion engineering or high electric fields can be used to control the amount of local charges and the various ionization and capture rates[198]. This can also be achieved with scanning tunnelling microscopy[212]. Finally, charge control can enable applications such as electrometry[199], super-resolution imaging[213] and control of defect formation kinetics[214].

In summary, the initialization and stabilization of the charge state of a defect is critical for high-fidelity

qubit operation. Controlling this property requires understanding the interplay between the charge state of each defect and the local charge trap environment, under electric fields and photoexcitation. As a guide, a key metric for charge stability is the bandgap of the host material, which should preferably be at least double the photoexcitation energy, and the position of charge transition levels for relevant defects. This stability is a major determining factor for the fidelity and noise present in quantum computation, communication and sensing applications.

Spin–charge interface. Readout for defect spins is not limited to ensemble spin resonance (inductive readout) or purely spin-dependent optical measurements. Spin-to-charge conversion (SCC) allows the spin state of a defect to be mapped to the presence or absence of charges. In the presence of an optical interface, SCC can proceed by the intermediary of spin-dependent optical processes. For defects without an optical interface, SCC can occur via recombination with nearby traps[48], by tunnelling to a quantum dot or reservoir of charges[14] or using polarized conduction electrons[215]. These processes are illustrated in FIG. 6d.

We first consider optically assisted SCC, where the large energy scales of optical excitations allow for SCC at elevated temperatures and low magnetic fields. This conversion utilizes spin-dependent photoionization with either spin-selective optical transitions[216] or spin-dependent shelving into metastable states (see the section on the spin–photon interface)[11,217]. Defects with bound exciton states near a band edge allow for SCC with spin-selective one-photon excitation into these states, followed by Auger recombination or thermal excitation[1,218]. One-photon SCC by direct excitation to a band is generally not possible, owing to the broadness of the transition compared with the spin's energy scales. Instead, two-photon excitation via an excited state provides another pathway for SCC, where either the first photon to the excited state is spin-selective or the absorption of the second photon occurs during a spin-dependent ISC decay. Generally, the ionization rate (second photon) should be fast compared with spin reinitialization during optical pumping.

SCC is also of interest for charge-selective optical readout, because the switchable charge states have distinct absorption and emission. With low optical power, this readout mechanism can probe the charge state of a defect, originally mapped from its spin state by the SCC, without causing further charge conversion. For defects without a good cycling transition or in cases of low collection efficiency, this method allows for high-fidelity measurement and, potentially, single-shot readout[216] or increased signal-to-noise ratio even at room temperature for quantum sensing[11].

SCC without optical assistance requires spin-dependent recombination or tunnelling mechanisms. Spin-dependent recombination with local traps, often dangling bonds at interfaces, relies on either thermal polarization of the spin, and, thus, large magnetic fields and low temperatures, or a relative spin polarization of the defect–trap pair (such as pairs that are randomly

either both spin up or both spin down), even at zero field and high temperature[219]. A related mechanism for both initialization and readout of defect spins is achieved by spin-dependent tunnelling to either a reservoir of charges or a quantum dot[14]. This mechanism requires low temperature and high magnetic fields, and is limited by the sharpness of the Fermi distribution of the electron reservoir[220]. This type of SCC allows for the use of hosts with smaller bandgaps through integration with electrical devices.

Independent of the SCC mechanism, electrical readout can occur through a variety of techniques (FIG. 6e). Spin-dependent readout can be directly performed via a photocurrent[221] or from fluctuations in the capacitance of a device due to changes in the trapped charge in a semiconductor[1]. Charge sensors such as single-electron transistors can measure single charges[14], so host crystals with this device capability are desired.

In summary, an efficient spin–charge interface enables new readout modalities for scaling in quantum computing, and can increase the spin readout signal for quantum sensing. This interface can be all electrical or optically assisted, which allows for high-temperature operation. In either case, guidelines include the need for a high-fidelity spin-dependent ionization process and a readout mechanism of defect charge states with single-shot compatibility. Finally, the ability to engineer the host material for integrated electrical devices will enable key technologies and applications.

Conclusions. Understanding and controlling the charge state of spin defects is critical to their operation in the solid state. This is achieved by combining knowledge of all impurities in the material with optical and electrical manipulation. Allowed optical transitions for both photoluminescence and ionization strongly influence the charge stability and depend on the position of the defect charge transition levels in the host bandgap. For scalability, electrical readout of the spin state can be achieved using spin-dependent ionization processes.

Material considerations

Spin defect qubit properties are interwoven with the intrinsic host material properties, including variations in crystallographic, dopant and nuclear-spin imperfections in their local environment. This demands consistently high-quality, low-strain and low-defect-density materials, possible in materials with mature synthesis and growth processes. Typical growth techniques include chemical vapour deposition and molecular beam epitaxy. More advanced methods such as the in situ incorporation of dopants with precise timing during growth and isotopic purification are also useful. The latter is conditional on the availability of nuclear-spin-free precursors.

The identification, creation and localization of defects remains a key challenge for the integration of these defects with optical devices, nanostructures and other spatially dependent applications. The ability to create localized defects must be achieved without introducing significant damage that would negatively affect the defect's spin, optical and charge properties.
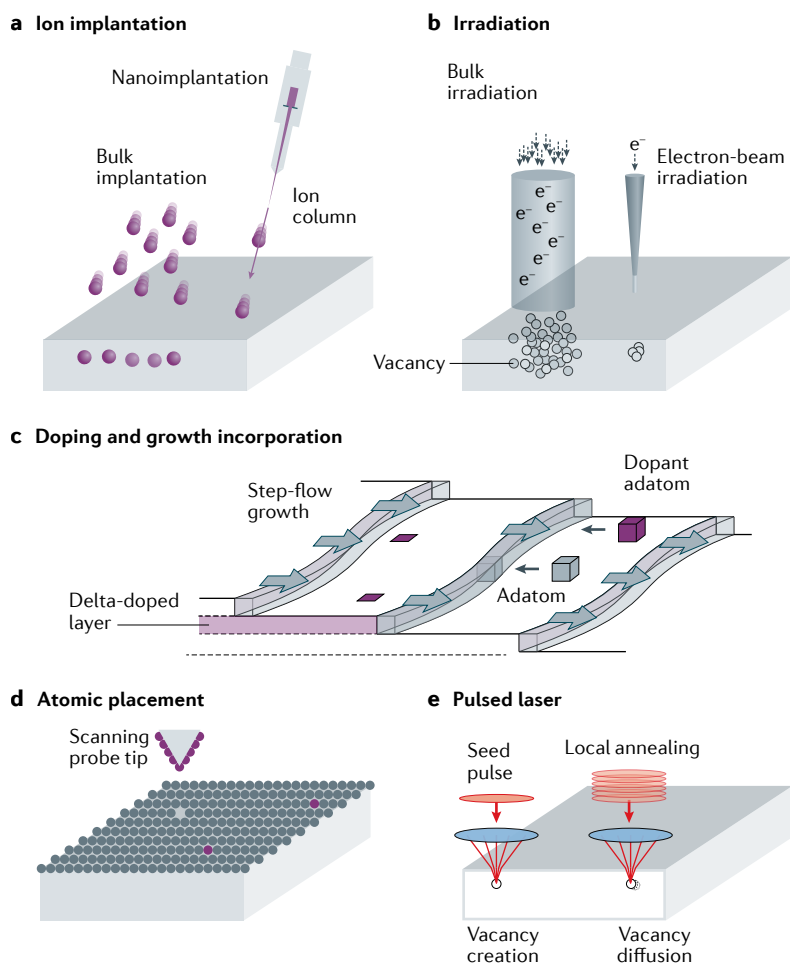
a Ion implantation

Nanoimplantation

Bulk
implantation

Ion
column

b Irradiation

Bulk
irradiation

e⁻ Electron-beam
irradiation

Vacancy

c Doping and growth incorporation

Dopant
adatom

Step-flow
growth

Adatom

Delta-doped
layer

d Atomic placement

Scanning
probe tip

e Pulsed laser

Seed
pulse

Local annealing

Vacancy
creation

Vacancy
diffusion

Fig. 7 | **Defect host material considerations. a** | Ion implantation can be used to create defects of many different species with a degree of depth localization. Implantation can be done via a bulk process or a nanoimplantation process using a modified focused ion beam[228,229]. **b** | Electron irradiation can be used to create vacancies either using bulk irradiation or using an electron beam for focused vacancy creation[232]. Although irradiation approaches offer a less precise depth localization, they typically create less damage to the crystal than ion implantation. **c** | Defects can be introduced during growth, which allows for careful control of the defect density, depth and local nuclear spin environment[130]. Growth methods can incorporate defects while maintaining a high crystal quality in the host material. **d** | Direct placement of atomic defects can be realized using a scanning probe tip[241]. **e** | Femtosecond pulse laser systems offer local vacancy creation (single seed pulse at higher laser intensity) and diffusion by annealing (multiple pulses at lower laser intensity). Panel **c** is adapted with permission from REF.[272].

Additionally, similar defect complexes can often exist in inequivalent lattice sites[45,175,222] and different crystallographic orientations[223], necessitating a detailed understanding of the defect orientation and spin Hamiltonian (for example, by combining theory, X-ray or ODMR experiments[223]).

A common way of creating high-quality spin defects is by starting with a low-defect-density material and introducing a controlled amount of the desired defects via growth, ion implantation, electron irradiation or impurity diffusion. Different considerations should be made depending on the defect species:

- Single-atomic defects, including substitutional defects such as P:Si, V:SiC and Er:Y_2SiO_5, can be introduced via ion implantation or through doping during growth, assuming that a suitable precursor growth chemistry is available.
- Atomic-vacancy defects such as NV:diamond and GeV:diamond similarly can be introduced via intentional doping during growth[130,224] or ion implantation[225]. The included vacancy adds complexity to the defect creation process and can be introduced concurrently with ion implantation or with additional electron irradiation.
- Vacancy complexes such as V_{Si}:SiC and VV:SiC are commonly introduced via electron irradiation (for singles), but can also be created via ion implantation.

Ion implantation is a versatile tool for creating defects (FIG. 7a) that offers the nearly full periodic spectrum of ions, though at the expense of crystallographic damage to the lattice, which can be partially mitigated with subsequent annealing and overgrowth[226]. Spatial (in-plane) localization can be achieved via aperture implantation[225,227] or nanoimplantation[228,229], and the depth can be predicted with Monte Carlo simulations[230]. Electron irradiation uses accelerated relativistic electrons to create vacancies uniformly throughout the sample (FIG. 7b). These particles primarily create single Frenkel defects in the lattice[231], in contrast to the cascades of defects created by ion implantation. This low-damage method is well suited to single defect creation, where improved spatial localization is achievable using transmission electron microscopy (TEM)[232] compared with bulk accelerators.

For single-atomic and atomic-vacancy complexes[130,233], a thin epitaxial layer can be grown with controlled doping density from precursor sources, including isotopic elements, and provides depth localization (within the 'delta-doped' layer) in a high-quality, low-strain crystal[234] (FIG. 7c). For atomic-vacancy defects, the combination of delta-doped growth and localized vacancy creation through aperture implantation[235] or TEM irradiation[232] can give the added benefit of full 3D positioning. Other growth techniques can also control the defect orientation through selective alignment during growth[236,237].

A final critical step is annealing to mobilize dopants and vacancies to create the desired defect. The annealing temperature and time necessary for specific defect formations are dictated by formation energies, migration mechanisms, doping defect densities (both intentional and naturally occurring), diffusion kinetics of impurities and defects[238], and the structure of the lattice. Likewise, annealing can improve the host's crystal quality and, therefore, the defect properties[239].

Alternative approaches towards localizing defects at the atomic scale have also been explored using scanning probe tips[240] (FIG. 7d) to position dopant defects in silicon[241,242] and 2D materials[243,244]. Such atomic localization becomes critical in device integration and for scaling up spin qubits. Likewise, the use of ultrafast pulsed lasers[245,246], X-ray beams and focused electron beams[232,247] has been explored to create local vacancies (FIG. 7b,e). Adding in situ monitoring of the luminescence from optical, X-ray or electron excitation provides real-time feedback in the defect creation process[247]. Likewise,

materials with mature electronics can be used to deterministically detect the implantation of single ions[248]. Furthermore, using rare isotopes during the creation of atomic-vacancy and substitutional defect complexes can help distinguish ('tag') those defects from naturally occurring ones[130,131]. Finally, defects can be randomly confined (sampled) into nanoscale volumes through integration with nanostructures (nanoparticles[249] and nanopillars[250,251]), embedded particle arrays[252], as well as by charge control and doping within electrical devices[198].

In summary, the selection of host materials should consider not only the properties of the spin defect but also the scalability (for example, wafer availability), ease of fabrication and unique properties (such as low acoustic loss) of the host. As a guide, key parameters for scalable implementation of defect-based quantum systems include the availability of highly crystalline, defect-free host materials and isotopically purified precursors for growth. Additionally, the ability to engineer the host material into photonic and electronic devices, as well as to create localized defects via pulsed laser, irradiation, implantation and growth, is critical to the successful amalgamation of defect and host material.

Outlook

Starting from initial experiments on spin coherence, every aspect of a defect and its host has now become relevant in the modern quantum context. Where some features may be lacking, the addition of material and device engineering, for example, with photonic, phononic or electrical devices and isotopically pure growth, can drastically improve the future viability of the defects.

The interplay between spin, optical, charge and material properties present a range of trade-offs to consider. The most fundamental balance is between control and coherence of the defect system for any parameter. A good compromise is for low sensitivity to sources of noise but high sensitivity to control and sensed fields. Electron and nuclear spin initialization, coherence and readout all require a spin–photon or spin–charge interface with opposing requirements for cyclicity (spin conservation). Material engineering, such as isotopic dilution or nanofabrication, comes with detrimental consequences, such as the loss of nuclear spin registers and increased surface noise or strain.

A variety of novel host materials can be identified according to their nuclear spin concentration, Debye temperature, bandgap, microwave or optical losses and many more relevant properties, as outlined in this guide. Beyond bulk materials, there is a growing interest in 2D materials[17] and molecular qubits[253,254] for bright, localized single-photon emitters[243], and new spin and optical tuning mechanisms.

The main challenge for the field is, therefore, finding a material host and defect for the specific application at hand. The major limitations for quantum communications are in creating indistinguishable photons at ideal wavelengths and in nanophotonic integration, whereas for quantum sensing, the signal-to-noise ratio and the effect of nearby surfaces determine the performance. Quantum computation faces the largest hurdles in terms of engineering interactions between nearby spins to create two-qubit gates.

Solid-state spin defects are already being deployed in commercial applications such as quantum sensing, and the continued progress and understanding of their interconnected properties is vital to fulfilling the full promise of defect-based quantum systems and their future in quantum communication, distributed quantum networks and other scalable quantum technologies.

1. Steger, M. et al. Quantum information storage for over 180 s using donor spins in a ^{28}Si "semiconductor vacuum". *Science* **336**, 1280–1283 (2012).
2. Gordon, J. P. & Bowers, K. D. Microwave spin echoes from donor electrons in silicon. *Phys. Rev. Lett.* **1**, 368–370 (1958).
3. Maiman, T. H. Stimulated optical radiation in ruby. *Nature* **187**, 493–494 (1960).
4. Abraham, M., Weeks, R. A., Clark, G. W. & Finch, C. B. Electron spin resonance of rare-earth ions in thorium oxide: Yb^{3+} and Er^{3+}. *Phys. Rev.* **137**, A138–A142 (1965).
5. Kane, B. E. A silicon-based nuclear spin quantum computer. *Nature* **393**, 133–137 (1998).
6. Ichimura, K. A simple frequency-domain quantum computer with ions in a crystal coupled to a cavity mode. *Opt. Commun.* **196**, 119–125 (2001).
7. Gruber, A. et al. Scanning confocal optical microscopy and magnetic resonance on single defect centers. *Science* **276**, 2012–2014 (1997).
8. Bradac, C., Gao, W., Forneris, J., Trusheim, M. E. & Aharonovich, I. Quantum nanophotonics with group IV defects in diamond. *Nat. Commun.* **10**, 5625 (2019).
9. Son, N. T. et al. Developing silicon carbide for quantum spintronics. *Appl. Phys. Lett.* **116**, 190501 (2020).
10. Barry, J. F. et al. Sensitivity optimization for NV-diamond magnetometry. *Rev. Mod. Phys.* **92**, 15004 (2020).
11. Jaskula, J. C. et al. Improved quantum sensing with a single solid-state spin via spin-to-charge conversion. *Phys. Rev. Appl.* **11**, 064003 (2019).
12. Bradley, C. E. et al. A ten-qubit solid-state spin register with quantum memory up to one minute. *Phys. Rev. X* **9**, 031045 (2019).
13. Simmons, S. et al. Entanglement in a solid-state spin ensemble. *Nature* **470**, 69–72 (2011).
14. Morello, A. et al. Single-shot readout of an electron spin in silicon. *Nature* **467**, 687–691 (2010).
15. Hensen, B. et al. Loophole-free Bell inequality violation using electron spins separated by 1.3 kilometres. *Nature* **526**, 682–686 (2015).
16. Wolfowicz, G. et al. Coherent storage of microwave excitations in rare-earth nuclear spins. *Phys. Rev. Lett.* **114**, 170503 (2015).
17. Toth, M. & Aharonovich, I. Single photon sources in atomically thin materials. *Annu. Rev. Phys. Chem.* **70**, 123–142 (2019).
18. Liu, X. & Hersam, M. C. 2D materials for quantum information science. *Nat. Rev. Mater.* **4**, 669–684 (2019).
19. Doherty, M. W. et al. The nitrogen-vacancy colour centre in diamond. *Phys. Rep.* **528**, 1–45 (2013).
20. Casola, F., van der Sar, T. & Yacoby, A. Probing condensed matter physics with magnetometry based on nitrogen-vacancy centres in diamond. *Nat. Rev. Mater.* **3**, 17088 (2018).
21. Lohrmann, A., Johnson, B. C., McCallum, J. C. & Castelletto, S. A review on single photon sources in silicon carbide. *Rep. Prog. Phys.* **80**, 034502 (2017).
22. Morley, G. W. Towards spintronic quantum technologies with dopants in silicon. *Electron. Paramagnetic Reson.* **24**, 62–76 (2015).
23. Zhong, T. & Goldner, P. Emerging rare-earth doped material platforms for quantum nanophotonics. *Nanophotonics* **8**, 2003–2015 (2019).
24. Ivády, V., Abrikosov, I. A. & Gali, A. First principles calculation of spin-related quantities for point defect qubit research. *NPJ Comput. Mater.* **4**, 76 (2018).
25. Heremans, F. J., Yale, C. G. & Awschalom, D. D. Control of spin defects in wide-bandgap semiconductors for quantum technologies. *Proc. IEEE* **104**, 2009–2023 (2016).
26. Bassett, L. C., Alkauskas, A., Exarhos, A. L. & Fu, K. C. Quantum defects by design. *Nanophotonics* **8**, 1867–1888 (2019).
27. Awschalom, D. D., Hanson, R., Wrachtrup, J. & Zhou, B. B. Quantum technologies with optically interfaced solid-state spins. *Nat. Photonics* **12**, 516–527 (2018).
28. Atatüre, M., Englund, D., Vamivakas, N., Lee, S.-Y. & Wrachtrup, J. Material platforms for spin-based photonic quantum technologies. *Nat. Rev. Mater.* **3**, 38–51 (2018).
29. Chatterjee, A. et al. Semiconductor qubits in practice. *Nat. Rev. Phys.* **3**, 157–177 (2021).
30. Jin, J. et al. Telecom-wavelength atomic quantum memory in optical fiber for heralded polarization qubits. *Phys. Rev. Lett.* **124**, 140501 (2019).
31. Tyryshkin, A. M., Lyon, S. A., Astashkin, A. V. & Raitsimring, A. M. Electron spin relaxation times of phosphorus donors in silicon. *Phys. Rev. B* **68**, 193207 (2003).
32. Bar-Gill, N., Pham, L. M., Jarmola, A., Budker, D. & Walsworth, R. L. Solid-state electronic spin coherence time approaching one second. *Nat. Commun.* **4**, 1743 (2013).
33. Gugler, J. et al. *Ab initio* calculation of the spin lattice relaxation time T_1 for nitrogen-vacancy centers in diamond. *Phys. Rev. B* **98**, 214442 (2018).
34. Norambuena, A. et al. Spin-lattice relaxation of individual solid-state spins. *Phys. Rev. B* **97**, 094304 (2018).
35. Shrivastava, K. N. Theory of spin–lattice relaxation. *Phys. Status Solidi* **117**, 437–458 (1983).
36. Abragam, A. & Bleaney, B. *Electron Paramagnetic Resonance of Transition Ions* (Oxford Univ. Press, 2012).
37. Jarmola, A., Acosta, V. M., Jensen, K., Chemerisov, S. & Budker, D. Temperature- and magnetic-field-dependent longitudinal spin relaxation in nitrogen-vacancy ensembles in diamond. *Phys. Rev. Lett.* **108**, 197601 (2012).

38. Castner, T. G. Raman spin-lattice relaxation of shallow donors in silicon. *Phys. Rev.* **130**, 58–75 (1963).
39. Green, B. L. et al. Neutral silicon-vacancy center in diamond: spin polarization and lifetimes. *Phys. Rev. Lett.* **119**, 096402 (2017).
40. Orbach, R. Spin-lattice relaxation in rare-earth salts. *Proc. R. Soc. Lond. A Math. Phys. Sci.* **264**, 458–484 (1961).
41. Xu, J. et al. Spin-phonon relaxation from a universal ab initio density-matrix approach. *Nat. Commun.* **11**, 2780 (2020).
42. Park, J., Zhou, J.-J. & Bernardi, M. Spin-phonon relaxation times in centrosymmetric materials from first principles. *Phys. Rev. B* **101**, 045202 (2020).
43. Kurkin, I. N. & Chernov, K. P. EPR and spin-lattice relaxation of rare-earth activated centres in Y_2SiO_5 single crystals. *Phys. B+C.* **101**, 233–238 (1980).
44. Meesala, S. et al. Strain engineering of the silicon-vacancy center in diamond. *Phys. Rev. B* **97**, 205444 (2018).
45. Wolfowicz, G. et al. Vanadium spin qubits as telecom quantum emitters in silicon carbide. *Sci. Adv.* **6**, eaaz1192 (2020).
46. Gilardoni, C. M. et al. Spin-relaxation times exceeding seconds for color centers with strong spin–orbit coupling in SiC. *New J. Phys.* **22**, 103051 (2020).
47. Kukharchyk, N., Sholokhov, D., Kalachev, A. A. & Bushev, P. A. Enhancement of optical coherence in $^{167}Er:Y_2SiO_5$ crystal at sub-Kelvin temperatures. Preprint at *arXiv* https://arxiv.org/abs/1910.03096 (2019).
48. Paik, S.-Y., Lee, S.-Y., Baker, W. J., McCamey, D. R. & Boehme, C. T_1 and T_2 spin relaxation time limitations of phosphorous donor electrons near crystalline silicon to silicon dioxide interface defects. *Phys. Rev. B* **81**, 075214 (2010).
49. Rosskopf, T. et al. Investigation of surface magnetic noise by shallow spins in diamond. *Phys. Rev. Lett.* **112**, 147602 (2014).
50. Myers, B. A. et al. Probing surface noise with depth-calibrated spins in diamond. *Phys. Rev. Lett.* **113**, 27602 (2014).
51. Sangtawesin, S. et al. Origins of diamond surface noise probed by correlating single-spin measurements with surface spectroscopy. *Phys. Rev. X* **9**, 031052 (2019).
52. Tetienne, J.-P. et al. Spin relaxometry of single nitrogen-vacancy defects in diamond nanocrystals for magnetic noise sensing. *Phys. Rev. B* **87**, 235436 (2013).
53. Ariyaratne, A., Bluvstein, D., Myers, B. A. & Jayich, A. C. B. Nanoscale electrical conductivity imaging using a nitrogen-vacancy center in diamond. *Nat. Commun.* **9**, 2406 (2018).
54. Morton, J. J. L. et al. Solid-state quantum memory using the ^{31}P nuclear spin. *Nature* **455**, 1085–1088 (2008).
55. Maurer, P. C. et al. Room-temperature quantum bit memory exceeding one second. *Science* **336**, 1283–1286 (2012).
56. Bienfait, A. et al. Controlling spin relaxation with a cavity. *Nature* **531**, 74–77 (2016).
57. Schweiger, A. & Jeschke, G. *Principles of Pulse Electron Paramagnetic Resonance* Vol. 4 (Oxford Univ. Press, 2001).
58. Tyryshkin, A. M. et al. Electron spin coherence exceeding seconds in high-purity silicon. *Nat. Mater.* **11**, 143–147 (2011).
59. Wolfowicz, G. et al. Atomic clock transitions in silicon-based spin qubits. *Nat. Nanotechnol.* **8**, 881–881 (2013).
60. Miao, K. C. et al. Universal coherence protection in a solid-state spin qubit. *Science* **369**, 1493–1497 (2020).
61. Yang, W. & Liu, R. Quantum many-body theory of qubit decoherence in a finite-size spin bath. II. Ensemble dynamics. *Phys. Rev. B* **79**, 115320 (2009).
62. Witzel, W. M. & Das Sarma, S. Quantum theory for electron spin decoherence induced by nuclear spin dynamics in semiconductor quantum computer architectures: Spectral diffusion of localized electron spins in the nuclear solid-state environment. *Phys. Rev. B* **74**, 035322 (2006).
63. Bar-Gill, N. et al. Suppression of spin-bath dynamics for improved coherence of multi-spin-qubit systems. *Nat. Commun.* **3**, 858 (2012).
64. Seo, H. et al. Quantum decoherence dynamics of divacancy spins in silicon carbide. *Nat. Commun.* **7**, 12935 (2016).
65. Balian, S. J., Wolfowicz, G., Morton, J. J. L. & Monteiro, T. S. Quantum-bath-driven decoherence of mixed spin systems. *Phys. Rev. B* **89**, 045403 (2014).

66. Kanai, S. et al. Generalized scaling of spin qubit coherence in over 12,000 host materials. Preprint at *arXiv* https://arxiv.org/abs/2102.02986 (2021).
67. Salikhov, K. M., Dzuba, S. A. & Raitsimring, A. M. The theory of electron spin-echo signal decay resulting from dipole-dipole interactions between paramagnetic centers in solids. *J. Magn. Reson.* **42**, 255–276 (1981).
68. Mims, W. B. Phase memory in electron spin echoes, lattice relaxation effects in CaWO₄: Er, Ce, Mn. *Phys. Rev.* **168**, 370–389 (1968).
69. Kukharchyk, N. et al. Optical coherence of $^{166}Er:^7LiYF_4$ crystal below 1 K. *New J. Phys.* **20**, 023044 (2018).
70. Car, B., Veissier, L., Louchet-Chauvet, A., Le Gouët, J. L. & Chanelière, T. Optical study of the anisotropic erbium spin flip-flop dynamics. *Phys. Rev. B* **100**, 165107 (2019).
71. Tosi, G. et al. Silicon quantum processor with robust long-distance qubit couplings. *Nat. Commun.* **8**, 450 (2017).
72. Ferrón, A., Rodríguez, S. A., Gómez, S. S., Lado, J. L. & Fernández-Rossier, J. Single spin resonance driven by electric modulation of the g-factor anisotropy. *Phys. Rev. Res.* **1**, 033185 (2019).
73. Park, D. K., Park, S., Jee, H. & Lee, S. Electron spin relaxations of phosphorus donors in bulk silicon under large electric field. *Sci. Rep.* **9**, 2951 (2019).
74. Kim, M. et al. Decoherence of near-surface nitrogen-vacancy centers due to electric field noise. *Phys. Rev. Lett.* **115**, 087602 (2015).
75. Rogers, L. J. et al. All-optical initialization, readout, and coherent preparation of single silicon-vacancy spins in diamond. *Phys. Rev. Lett.* **113**, 263602 (2014).
76. Witzel, W. M., Carroll, M. S., Morello, A., Cywiński, Ł. & Das Sarma, S. Electron spin decoherence in isotope-enriched silicon. *Phys. Rev. Lett.* **105**, 187602 (2010).
77. Bourassa, A. et al. Entanglement and control of single nuclear spins in isotopically engineered silicon carbide. *Nat. Mater.* **19**, 1319–1325 (2020).
78. Balasubramanian, G. et al. Ultralong spin coherence time in isotopically engineered diamond. *Nat. Mater.* **8**, 383–387 (2009).
79. Ye, M., Seo, H. & Galli, G. Spin coherence in two-dimensional materials. *NPJ Comput. Mater.* **5**, 44 (2019).
80. Abe, E., Itoh, K. M., Isoya, J. & Yamasaki, S. Electron-spin phase relaxation of phosphorus donors in nuclear-spin-enriched silicon. *Phys. Rev. B* **70**, 033204 (2004).
81. Longdell, J. J., Alexander, A. L. & Sellars, M. J. Characterization of the hyperfine interaction in europium-doped yttrium orthosilicate and europium chloride hexahydrate. *Phys. Rev. B* **74**, 195101 (2006).
82. McAuslan, D. L., Bartholomew, J. G., Sellars, M. J. & Longdell, J. J. Reducing decoherence in optical and spin transitions in rare-earth-metal-ion–doped materials. *Phys. Rev. A* **85**, 032339 (2012).
83. Onizhuk, M. et al. Probing the coherence of solid-state qubits at avoided crossings. *PRX Quantum* **2**, 010311 (2021).
84. Parker, A. J., Wang, H.-J., Li, Y., Pines, A. & King, J. P. Decoherence-protected transitions of nitrogen vacancy centers in 99% 13C-enriched diamond. Preprint at *arXiv* https://arxiv.org/abs/1506.05484 (2015).
85. Barfuss, A., Teissier, J., Neu, E., Nunnenkamp, A. & Maletinsky, P. Strong mechanical driving of a single electron spin. *Nat. Phys.* **11**, 820–824 (2015).
86. Stark, A. et al. Clock transition by continuous dynamical decoupling of a three-level system. *Sci. Rep.* **8**, 14807 (2018).
87. Viola, L., Knill, E. & Lloyd, S. Dynamical decoupling of open quantum systems. *Phys. Rev. Lett.* **82**, 2417–2421 (1999).
88. Bylander, J. et al. Noise spectroscopy through dynamical decoupling with a superconducting flux qubit. *Nat. Phys.* **7**, 565–570 (2011).
89. Wang, Z.-H., de Lange, G., Ristè, D., Hanson, R. & Dobrovitski, V. V. Comparison of dynamical decoupling protocols for a nitrogen-vacancy center in diamond. *Phys. Rev. B* **85**, 155204 (2012).
90. Pickard, C. J. & Mauri, F. First-principles theory of the EPR *g* tensor in solids: defects in quartz. *Phys. Rev. Lett.* **88**, 086403 (2002).
91. Pfanner, G., Freysoldt, C., Neugebauer, J. & Gerstmann, U. *Ab initio* EPR parameters for dangling-bond defect complexes in silicon: Effect of Jahn-Teller distortion. *Phys. Rev. B* **85**, 195202 (2012).
92. Gali, A., Fyta, M. & Kaxiras, E. *Ab initio* supercell calculations on nitrogen-vacancy center in diamond: Electronic structure and hyperfine tensors. *Phys. Rev. B* **77**, 155206 (2008).

93. Seo, H., Ma, H., Govoni, M. & Galli, G. Designing defect-based qubit candidates in wide-gap binary semiconductors for solid-state quantum technologies. *Phys. Rev. Mater.* **1**, 075002 (2017).
94. Ghosh, K., Ma, H., Gavini, V. & Galli, G. All-electron density functional calculations for electron and nuclear spin interactions in molecules and solids. *Phys. Rev. Mater.* **3**, 043801 (2019).
95. Bodrog, Z. & Gali, A. The spin–spin zero-field splitting tensor in the projector-augmented-wave method. *J. Phys. Condens. Matter* **26**, 015305 (2014).
96. Pica, G. et al. Hyperfine Stark effect of shallow donors in silicon. *Phys. Rev. B* **90**, 195204 (2014).
97. Whiteley, S. J. et al. Spin–phonon interactions in silicon carbide addressed by Gaussian acoustics. *Nat. Phys.* **15**, 490–495 (2019).
98. Kramers, H. A. Théorie générale de la rotation paramagnetique dans les cristaux. *Proc. Acad. Amst.* **33**, 959–972 (1930).
99. Udvarhelyi, P., Shkolnikov, V. O., Gali, A., Burkard, G. & Pályi, A. Spin-strain interaction in nitrogen-vacancy centers in diamond. *Phys. Rev. B* **98**, 075201 (2018).
100. Rao, K. R. K. & Suter, D. Nonlinear dynamics of a two-level system of a single spin driven beyond the rotating-wave approximation. *Phys. Rev. A* **95**, 053804 (2017).
101. Laucht, A. et al. Electrically controlling single-spin qubits in a continuous microwave field. *Sci. Adv.* **1**, e1500022 (2015).
102. Dreher, L. et al. Electroelastic hyperfine tuning of phosphorus donors in silicon. *Phys. Rev. Lett.* **106**, 037601 (2011).
103. Klimov, P. V., Falk, A. L., Buckley, B. B. & Awschalom, D. D. Electrically driven spin resonance in silicon carbide color centers. *Phys. Rev. Lett.* **112**, 087601 (2014).
104. Asaad, S. et al. Coherent electrical control of a single high-spin nucleus in silicon. *Nature* **579**, 205–209 (2020).
105. Maity, S. et al. Coherent acoustic control of a single silicon vacancy spin in diamond. *Nat. Commun.* **11**, 193 (2020).
106. Neuman, T. et al. A phononic bus for coherent interfaces between a superconducting quantum processor, spin memory, and photonic quantum networks. Preprint at *arXiv* https://arxiv.org/abs/2003.08383 (2020).
107. Khaneja, N., Reiss, T., Kehlet, C., Schulte-Herbrüggen, T. & Glaser, S. J. Optimal control of coupled spin dynamics: Design of NMR pulse sequences by gradient ascent algorithms. *J. Magn. Reson.* **172**, 296–305 (2005).
108. Tannús, A. & Garwood, M. Adiabatic pulses. *NMR Biomed.* **10**, 423–434 (1997).
109. Wimperis, S. Broadband, narrowband, and passband composite pulses for use in advanced NMR experiments. *J. Magn. Reson. A* **109**, 221–231 (1994).
110. Leibfried, D., Blatt, R., Monroe, C. & Wineland, D. Quantum dynamics of single trapped ions. *Rev. Mod. Phys.* **75**, 281–324 (2003).
111. Bergmann, K., Theuer, H. & Shore, B. W. Coherent population transfer among quantum states of atoms and molecules. *Rev. Mod. Phys.* **70**, 1003–1025 (1998).
112. Baldit, E. et al. Identification of Λ-like systems in $Er^{3+}:Y_2SiO_5$ and observation of electromagnetically induced transparency. *Phys. Rev. B* **81**, 144303 (2010).
113. Yale, C. G. et al. Optical manipulation of the Berry phase in a solid-state spin qubit. *Nat. Photonics* **10**, 184–189 (2016).
114. Yale, C. G. et al. All-optical control of a solid-state spin using coherent dark states. *Proc. Natl Acad. Sci. USA* **110**, 7595–7600 (2013).
115. Zwier, O. V., O'Shea, D., Onur, A. R. & van der Wal, C. H. All-optical coherent population trapping with defect spin ensembles in silicon carbide. *Sci. Rep.* **5**, 10931 (2015).
116. Evans, R. E. et al. Photon-mediated interactions between quantum emitters in a diamond nanocavity. *Science* **362**, 662–665 (2018).
117. Zhou, B. B. et al. Holonomic quantum control by coherent optical excitation in diamond. *Phys. Rev. Lett.* **119**, 140503 (2017).
118. Sekiguchi, Y., Niikura, N., Kuroiwa, R., Kano, H. & Kosaka, H. Optical holonomic single quantum gates with a geometric spin under a zero field. *Nat. Photonics* **11**, 309–314 (2017).
119. Zhou, B. B. et al. Accelerated quantum control using superadiabatic dynamics in a solid-state lambda system. *Nat. Phys.* **13**, 330–334 (2017).

120. Bersin, E. et al. Individual control and readout of qubits in a sub-diffraction volume. *NPJ Quantum Inf.* **5**, 39 (2019).

121. Chen, S., Raha, M., Phenicie, C. M., Ourari, S. & Thompson, J. D. Parallel single-shot measurement and coherent control of solid-state spins below the diffraction limit. *Science* **370**, 592–595 (2020).

122. Reiserer, A. et al. Robust quantum-network memory using decoherence-protected subspaces of nuclear spins. *Phys. Rev. X* **6**, 021040 (2016).

123. Kalb, N. et al. Entanglement distillation between solid-state quantum network nodes. *Science* **356**, 928–932 (2017).

124. Waldherr, G. et al. Quantum error correction in a solid-state hybrid spin register. *Nature* **506**, 204–207 (2014).

125. Taminiau, T. H., Cramer, J., Van Der Sar, T., Dobrovitski, V. V. & Hanson, R. Universal control and error correction in multi-qubit spin registers in diamond. *Nat. Nanotechnol.* **9**, 171–176 (2014).

126. Zaiser, S. et al. Enhancing quantum sensing sensitivity by a quantum memory. *Nat. Commun.* **7**, 12279 (2016).

127. Saeedi, K. et al. Room-temperature quantum bit storage exceeding 39 minutes using ionized donors in silicon-28. *Science* **342**, 830–833 (2013).

128. Hartman, J. S. et al. NMR studies of nitrogen doping in the 4H polytype of silicon carbide: Site assignments and spin–lattice relaxation. *J. Phys. Chem. C* **113**, 15024–15036 (2009).

129. Bergeron, L. et al. Characterization of the T center in ^{28}Si. Preprint at *arxiv* https://arxiv.org/abs/2006.08794 (2020).

130. Ohno, K. et al. Engineering shallow spins in diamond with nitrogen delta-doping. *Appl. Phys. Lett.* **101**, 082413 (2012).

131. Rabeau, J. R. et al. Implantation of labelled single nitrogen vacancy centers in diamond using ^{15}N. *Appl. Phys. Lett.* **88**, 023113 (2006).

132. Wolfowicz, G. et al. Decoherence mechanisms of ^{209}Bi donor electron spins in isotopically pure ^{28}Si. *Phys. Rev. B* **86**, 245301 (2012).

133. Taminiau, T. H. et al. Detection and control of individual nuclear spins using a weakly coupled electron spin. *Phys. Rev. Lett.* **109**, 137602 (2012).

134. Kolkowitz, S., Unterreithmeier, Q. P., Bennett, S. D. & Lukin, M. D. Sensing distant nuclear spins with a single electron spin. *Phys. Rev. Lett.* **109**, 137601 (2012).

135. Abobeih, M. H. et al. Atomic-scale imaging of a 27-nuclear-spin cluster using a quantum sensor. *Nature* **576**, 411–415 (2019).

136. Zhao, N. et al. Sensing single remote nuclear spins. *Nat. Nanotechnol.* **7**, 657–662 (2012).

137. Guichard, R., Balian, S. J., Wolfowicz, G., Mortemousque, P. A. & Monteiro, T. S. Decoherence of nuclear spins in the frozen core of an electron spin. *Phys. Rev. B* **91**, 214303 (2015).

138. Kalb, N., Humphreys, P. C., Slim, J. J. & Hanson, R. Dephasing mechanisms of diamond-based nuclear-spin memories for quantum networks. *Phys. Rev. A* **97**, 062330 (2018).

139. Blok, M. S., Kalb, N., Reiserer, A., Taminiau, T. H. & Hanson, R. Towards quantum networks of single spins: analysis of a quantum memory with an optical interface in diamond. *Faraday Discuss.* **184**, 173–182 (2015).

140. Mądzik, M. T. et al. Controllable freezing of the nuclear spin bath in a single-atom spin qubit. *Sci. Adv.* **6**, eaba3442 (2020).

141. Itoh, K. M. & Watanabe, H. Isotope engineering of silicon and diamond for quantum computing and sensing applications. *MRS Commun.* **4**, 143–157 (2014).

142. Dibos, A. M., Raha, M., Phenicie, C. M. & Thompson, J. D. Atomic source of single photons in the telecom band. *Phys. Rev. Lett.* **120**, 243601 (2018).

143. Spindlberger, L. et al. Optical properties of vanadium in 4H silicon carbide for quantum technology. *Phys. Rev. Appl.* **12**, 014015 (2019).

144. Smith, A. M., Mancini, M. C. & Nie, S. Bioimaging: Second window for in vivo imaging. *Nat. Nanotechnol.* **4**, 710–711 (2009).

145. Drĕau, A. et al. Quantum frequency conversion of single photons from a nitrogen-vacancy center in diamond to telecommunication wavelengths. *Phys. Rev. Appl.* **9**, 064031 (2018).

146. Pelc, J. S., Langrock, C., Zhang, Q. & Fejer, M. M. Influence of domain disorder on parametric noise in quasi-phase-matched quantum frequency converters. *Opt. Lett.* **35**, 2804 (2010).

147. Kumar, P. Quantum frequency conversion. *Opt. Lett.* **15**, 1476 (1990).

148. Siyushev, P. et al. Monolithic diamond optics for single photon detection. *Appl. Phys. Lett.* **97**, 241902 (2010).

149. Huang, T. Y. et al. A monolithic immersion metalens for imaging solid-state quantum emitters. *Nat. Commun.* **10**, 2392 (2019).

150. Butcher, A. et al. High-*Q* nanophotonic resonators on diamond membranes using templated atomic layer deposition of TiO$_2$. *Nano Lett.* **20**, 4603–4609 (2020).

151. Norman, V. A. et al. Novel color center platforms enabling fundamental scientific discovery. *InfoMat* https://doi.org/10.1002/inf2.12128 (2020).

152. Kim, J.-H., Aghaeimeibodi, S., Carolan, J., Englund, D. & Waks, E. Hybrid integration methods for on-chip quantum photonics. *Optica* **7**, 291–308 (2020).

153. Crook, A. L. et al. Purcell enhancement of a single silicon carbide color center with coherent spin control. *Nano Lett.* **20**, 3427–3434 (2020).

154. Huang, K. & Rhys, A. Theory of light absorption and non-radiative transitions in *F*-centres. *Proc. R. Soc. Lond. A Math. Phys. Sci.* **204**, 406–423 (1950).

155. Udvarhelyi, P. et al. Vibronic states and their effect on the temperature and strain dependence of silicon-vacancy qubits in 4H-SiC. *Phys. Rev. Appl.* **13**, 054017 (2020).

156. Alkauskas, A., Buckley, B. B., Awschalom, D. D. & Van de Walle, C. G. First-principles theory of the luminescence lineshape for the triplet transition in diamond NV centres. *New J. Phys.* **16**, 073026 (2014).

157. Gali, A., Simon, T. & Lowther, J. E. An ab initio study of local vibration modes of the nitrogen-vacancy center in diamond. *New J. Phys.* **13**, 025016 (2011).

158. Kindem, J. M. et al. Control and single-shot readout of an ion embedded in a nanophotonic cavity. *Nature* **580**, 201–204 (2020).

159. Raha, M. et al. Optical quantum nondemolition measurement of a single rare earth ion qubit. *Nat. Commun.* **11**, 1605 (2020).

160. Bockstedte, M., Schütz, F., Garratt, T., Ivády, V. & Gali, A. Ab initio description of highly correlated states in defects for realizing quantum bits. *NPJ Quantum Mater.* **3**, 31 (2018).

161. Christle, D. J. et al. Isolated spin qubits in SiC with a high-fidelity infrared spin-to-photon interface. *Phys. Rev. X* **7**, 021046 (2017).

162. Radko, I. P. et al. Determining the internal quantum efficiency of shallow-implanted nitrogen-vacancy defects in bulk diamond. *Opt. Express* **24**, 27715 (2016).

163. Gali, Á. Ab initio theory of the nitrogen-vacancy center in diamond. *Nanophotonics* **8**, 1907–1943 (2019).

164. Lannoo, M. & Bourgoin, J. *Point Defects in Semiconductors I. Springer Series in Solid-State Sciences* Vol. 22 36–67 (Springer, 1981).

165. Koehl, W. F. et al. Resonant optical spectroscopy and coherent control of Cr^{4+} spin ensembles in SiC and GaN. *Phys. Rev. B* **95**, 035207 (2017).

166. Laporte, O. & Meggers, W. F. Some rules of spectral structure. *J. Opt. Soc. Am.* **11**, 459–463 (1925).

167. Seo, H., Govoni, M. & Galli, G. Design of defect spins in piezoelectric aluminum nitride for solid-state hybrid quantum technologies. *Sci. Rep.* **6**, 20803 (2016).

168. Ma, H., Govoni, M. & Galli, G. Quantum simulations of materials on near-term quantum computers. *NPJ Comput. Mater.* **6**, 85 (2020).

169. Bosma, T. et al. Identification and tunable optical coherent control of transition-metal spins in silicon carbide. *NPJ Quantum Inf.* **4**, 48 (2018).

170. Tanabe, Y. & Sugano, S. On the absorption spectra of complex ions II. *J. Phys. Soc. Jpn.* **9**, 766–779 (1954).

171. Tanabe, Y. & Sugano, S. On the absorption spectra of complex ions. I. *J. Phys. Soc. Jpn.* **9**, 753–766 (1954).

172. Togan, E. et al. Quantum entanglement between an optical photon and a solid-state spin qubit. *Nature* **466**, 730–734 (2010).

173. Müller, T. et al. Optical signatures of silicon-vacancy spins in diamond. *Nat. Commun.* **5**, 3328 (2014).

174. Nagy, R. et al. High-fidelity spin and optical control of single silicon-vacancy centres in silicon carbide. *Nat. Commun.* **10**, 1954 (2019).

175. Diler, B. et al. Coherent control and high-fidelity readout of chromium ions in commercial silicon carbide. *NPJ Quantum Inf.* **6**, 11 (2020).

176. Acosta, V. M. et al. Dynamic stabilization of the optical resonances of single nitrogen-vacancy centers in diamond. *Phys. Rev. Lett.* **108**, 206401 (2012).

177. Robledo, L. et al. High-fidelity projective read-out of a solid-state spin quantum register. *Nature* **477**, 574–578 (2011).

178. Manson, N. B., Sellars, M. J., Fisk, P. T. H. & Meltzer, R. S. Hole burning of rare earth ions with kHz resolution. *J. Lumin.* **64**, 19–23 (1995).

179. Zhong, T. et al. Nanophotonic rare-earth quantum memory with optically controlled retrieval. *Science* **357**, 1392–1395 (2017).

180. Biktagirov, T. & Gerstmann, U. Spin-orbit driven electrical manipulation of the zero-field splitting in high-spin centers in solids. *Phys. Rev. Res.* **2**, 023071 (2020).

181. Thiering, G. & Gali, A. *Ab initio* calculation of spin-orbit coupling for an NV center in diamond exhibiting dynamic Jahn-Teller effect. *Phys. Rev. B* **96**, 081115 (2017).

182. Goldman, M. L. et al. Phonon-induced population dynamics and intersystem crossing in nitrogen-vacancy centers. *Phys. Rev. Lett.* **114**, 145502 (2015).

183. Thiering, G. & Gali, A. Theory of the optical spin-polarization loop of the nitrogen-vacancy center in diamond. *Phys. Rev. B* **98**, 085207 (2018).

184. Dong, W., Doherty, M. W. & Economou, S. E. Spin polarization through intersystem crossing in the silicon vacancy of silicon carbide. *Phys. Rev. B* **99**, 184102 (2019).

185. Toyli, D. M. et al. Measurement and control of single nitrogen-vacancy center spins above 600 K. *Phys. Rev. X* **2**, 031001 (2012).

186. Hopper, D., Shulevitz, H. & Bassett, L. Spin readout techniques of the nitrogen-vacancy center in diamond. *Micromachines* **9**, 437 (2018).

187. Bonato, C. et al. Optimized quantum sensing with a single electron spin using real-time adaptive measurements. *Nat. Nanotechnol.* **11**, 247–252 (2016).

188. Bernien, H. et al. Heralded entanglement between solid-state qubits separated by three metres. *Nature* **497**, 86–90 (2013).

189. Kambs, B. & Becher, C. Limitations on the indistinguishability of photons from remote solid state sources. *New J. Phys.* **20**, 115003 (2018).

190. Miao, K. C. et al. Electrically driven optical interferometry with spins in silicon carbide. *Sci. Adv.* **5**, eaay0527 (2019).

191. Hong, C. K., Ou, Z. Y. & Mandel, L. Measurement of subpicosecond time intervals between two photons by interference. *Phys. Rev. Lett.* **59**, 2044–2046 (1987).

192. Humphreys, P. C. et al. Deterministic delivery of remote entanglement on a quantum network. *Nature* **558**, 268–273 (2018).

193. Jahnke, K. D. et al. Electron–phonon processes of the silicon-vacancy centre in diamond. *New J. Phys.* **17**, 043011 (2015).

194. Fu, K.-M. C. et al. Observation of the dynamic Jahn-Teller effect in the excited states of nitrogen-vacancy centers in diamond. *Phys. Rev. Lett.* **103**, 256404 (2009).

195. Böttger, T., Thiel, C. W., Sun, Y. & Cone, R. L. Optical decoherence and spectral diffusion at 1.5 μm in Er^{3+}:Y$_2$SiO$_5$ versus magnetic field, temperature, and Er^{3+} concentration. *Phys. Rev. B* **73**, 075101 (2006).

196. Cardona, M. & Thewalt, M. L. W. Isotope effects on the optical spectra of semiconductors. *Rev. Mod. Phys.* **77**, 1173–1224 (2005).

197. Macfarlane, R. M., Cassanho, A. & Meltzer, R. S. Inhomogeneous broadening by nuclear spin fields: A new limit for optical transitions in solids. *Phys. Rev. Lett.* **69**, 542–545 (1992).

198. Anderson, C. P. et al. Electrical and optical control of single spins integrated in scalable semiconductor devices. *Science* **366**, 1225–1230 (2019).

199. Wolfowicz, G., Whiteley, S. J. & Awschalom, D. D. Electrometry by optical charge conversion of deep defects in 4H-SiC. *Proc. Natl Acad. Sci. USA* **115**, 7879–7883 (2018).

200. Bassett, L. C., Heremans, F. J., Yale, C. G., Buckley, B. B. & Awschalom, D. D. Electrical tuning of single nitrogen-vacancy center optical transitions enhanced by photoinduced fields. *Phys. Rev. Lett.* **107**, 266403 (2011).

201. Anderson, C. P. *Spin Qubits in Silicon Carbide Electronic Devices*. PhD thesis, Univ. Chicago (2020).

202. Candido, D. R. & Flatté, M. E. Suppression of the optical linewidth and spin decoherence of a quantum spin center in a *p–n* diode. Preprint at *arXiv* https://arxiv.org/abs/2008.13289 (2020).

203. Sipahigil, A. et al. Indistinguishable photons from separated silicon-vacancy centers in diamond. *Phys. Rev. Lett.* **113**, 113602 (2014).

204. Schmidgall, E. R. et al. Frequency control of single quantum emitters in integrated photonic circuits. *Nano Lett.* **18**, 1175–1179 (2018).

205. Giri, R. et al. Coupled charge and spin dynamics in high-density ensembles of nitrogen-vacancy centers in diamond. *Phys. Rev. B* **98**, 045401 (2018).

206. Scherpelz, P. & Galli, G. Optimizing surface defects for atomic-scale electronics: Si dangling bonds. *Phys. Rev. Mater.* **1**, 021602 (2017).

207. Wickramaratne, D. et al. Defect identification based on first-principles calculations for deep level transient spectroscopy. *Appl. Phys. Lett.* **113**, 192106 (2018).

208. Wolfowicz, G. et al. Optical charge state control of spin defects in 4H-SiC. *Nat. Commun.* **8**, 1876 (2017).

209. Jayakumar, H. et al. Optical patterning of trapped charge in nitrogen-doped diamond. *Nat. Commun.* **7**, 12660 (2016).

210. Isoya, J. et al. EPR identification of intrinsic defects in SiC. *Phys. Status Solidi* **245**, 1298–1314 (2008).

211. Aslam, N., Waldherr, G., Neumann, P., Jelezko, F. & Wrachtrup, J. Photo-induced ionization dynamics of the nitrogen vacancy defect in diamond investigated by single-shot charge state detection. *New J. Phys.* **15**, 013064 (2013).

212. Wong, D. et al. Characterization and manipulation of individual defects in insulating hexagonal boron nitride using scanning tunnelling microscopy. *Nat. Nanotechnol.* **10**, 949–953 (2015).

213. Han, K. Y., Kim, S. K., Eggeling, C. & Hell, S. W. Metastable dark states enable ground state depletion microscopy of nitrogen vacancy centers in diamond with diffraction-unlimited resolution. *Nano Lett.* **10**, 3199–3203 (2010).

214. Fávaro de Oliveira, F. et al. Tailoring spin defects in diamond by lattice charging. *Nat. Commun.* **8**, 15409 (2017).

215. Lo, C. C. et al. Electrically detected magnetic resonance of neutral donors interacting with a two-dimensional electron gas. *Phys. Rev. Lett.* **106**, 207601 (2011).

216. Irber, D. M. et al. Robust all-optical single-shot readout of NV centers in diamond. Preprint at *arXiv* https://arxiv.org/abs/2006.02938 (2020).

217. Shields, B. J., Unterreithmeier, Q. P., De Leon, N. P., Park, H. & Lukin, M. D. Efficient readout of a single spin state in diamond via spin-to-charge conversion. *Phys. Rev. Lett.* **114**, 136402 (2015).

218. Lo, C. C. et al. Hybrid optical–electrical detection of donor electron spins with bound excitons in silicon. *Nat. Mater.* **14**, 490–494 (2015).

219. Hoehne, F., Huebl, H., Galler, B., Stutzmann, M. & Brandt, M. S. Spin-dependent recombination between phosphorus donors in silicon and Si/SiO$_2$ interface states investigated with pulsed electrically detected electron double resonance. *Phys. Rev. Lett.* **104**, 046402 (2010).

220. Elzerman, J. M. et al. Single-shot read-out of an individual electron spin in a quantum dot. *Nature* **430**, 431–435 (2004).

221. Siyushev, P. et al. Photoelectrical imaging and coherent spin-state readout of single nitrogen-vacancy centers in diamond. *Science* **363**, 728–731 (2019).

222. Falk, A. L. et al. Polytype control of spin qubits in silicon carbide. *Nat. Commun.* **4**, 1819 (2013).

223. Doherty, M. W. et al. Measuring the defect structure orientation of a single NV$^-$ centre in diamond. *New J. Phys.* **16**, 063067 (2014).

224. Westerhausen, M. T. et al. Controlled doping of GeV and SnV color centers in diamond using chemical vapor deposition. *ACS Appl. Mater. Interfaces* **12**, 29700–29705 (2020).

225. Toyli, D. M., Weis, C. D., Fuchs, G. D., Schenkel, T. & Awschalom, D. D. Chip-scale nanofabrication of single spins and spin arrays in diamond. *Nano Lett.* **10**, 3168–3172 (2010).

226. Rugar, A. E. et al. Generation of tin-vacancy centers in diamond via shallow ion implantation and subsequent diamond overgrowth. *Nano Lett.* **20**, 1614–1619 (2020).

227. Scarabelli, D., Trusheim, M., Gaathon, O., Englund, D. & Wind, S. J. Nanoscale engineering of closely-spaced electronic spins in diamond. *Nano Lett.* **16**, 4982–4990 (2016).

228. Wan, N. H. et al. Large-scale integration of artificial atoms in hybrid photonic circuits. *Nature* **583**, 226–231 (2020).

229. Schröder, T. et al. Scalable focused ion beam creation of nearly lifetime-limited single quantum emitters in diamond nanostructures. *Nat. Commun.* **8**, 15376 (2017).

230. Ziegler, J. F. & Biersack, J. P. in *Treatise on Heavy-Ion Science* (eds. Bromley, D. A.) 93–129 (Springer, 1985).

231. Lebedev, A. A. *Radiation Effects in Silicon Carbide* (Materials Research Forum, 2017).

232. McLellan, C. A. et al. Patterned formation of highly coherent nitrogen-vacancy centers using a focused electron irradiation technique. *Nano Lett.* **16**, 2450–2454 (2016).

233. Singh, M. K. et al. Epitaxial Er-doped Y$_2$O$_3$ on silicon for quantum coherent devices. *APL Mater.* **8**, 031111 (2020).

234. Jaffe, T. et al. Novel ultra localized and dense nitrogen delta-doping in diamond for advanced quantum sensing. *Nano Lett.* **20**, 3192–3198 (2020).

235. Ohno, K. et al. Three-dimensional localization of spins in diamond using ^{12}C implantation. *Appl. Phys. Lett.* **105**, 052406 (2014).

236. Lesik, M. et al. Perfect preferential orientation of nitrogen-vacancy defects in a synthetic diamond sample. *Appl. Phys. Lett.* **104**, 113107 (2014).

237. Michl, J. et al. Perfect alignment and preferential orientation of nitrogen-vacancy centers during chemical vapor deposition diamond growth on (111) surfaces. *Appl. Phys. Lett.* **104**, 102407 (2014).

238. Chakravarthi, S. et al. Window into NV center kinetics via repeated annealing and spatial tracking of thousands of individual NV centers. *Phys. Rev. Mater.* **4**, 023402 (2020).

239. Hruszkewycz, S. O. et al. Strain annealing of SiC nanoparticles revealed through Bragg coherent diffraction imaging for quantum technologies. *Phys. Rev. Mater.* **2**, 086001 (2018).

240. Lee, D. & Gupta, J. A. Perspectives on deterministic control of quantum point defects by scanned probes. *Nanophotonics* **8**, 2033–2040 (2019).

241. Schofield, S. R. et al. Atomically precise placement of single dopants in Si. *Phys. Rev. Lett.* **91**, 136104 (2003).

242. Stock, T. J. Z. et al. Atomic-scale patterning of arsenic in silicon by scanning tunneling microscopy. *ACS Nano* **14**, 3316–3327 (2020).

243. Schuler, B. et al. How substitutional point defects in two-dimensional WS$_2$ induce charge localization, spin–orbit splitting, and strain. *ACS Nano* **13**, 10520–10534 (2019).

244. Mitterreiter, E. et al. Atomistic positioning of defects in helium ion treated single-layer MoS$_2$. *Nano Lett.* **20**, 4437–4444 (2020).

245. Kurita, T. et al. Efficient generation of nitrogen-vacancy center inside diamond with shortening of laser pulse duration. *Appl. Phys. Lett.* **113**, 211102 (2018).

246. Chen, Y.-C. et al. Laser writing of individual nitrogen-vacancy defects in diamond with near-unity yield. *Optica* **6**, 662–667 (2019).

247. Smith, J. M., Meynell, S. A., Jayich, A. C. B. & Meijer, J. Colour centre generation in diamond for quantum technologies. *Nanophotonics* **8**, 1889–1906 (2019).

248. Jakob, A. M. et al. Deterministic single ion implantation with 99.87% confidence for scalable donor-qubit arrays in silicon. Preprint at *arXiv* https://arxiv.org/abs/2009.02892 (2020).

249. Andrich, P. et al. Engineered micro- and nanoscale diamonds as mobile probes for high-resolution sensing in fluid. *Nano Lett.* **14**, 4959–4964 (2014).

250. Momenzadeh, S. A. et al. Nanoengineered diamond waveguide as a robust bright platform for nanomagnetometry using shallow nitrogen vacancy centers. *Nano Lett.* **15**, 165–169 (2015).

251. Widmann, C. J. et al. Fabrication and characterization of single crystalline diamond nanopillars with NV-centers. *Diam. Relat. Mater.* **54**, 2–8 (2015).

252. Andrich, P. et al. Microscale-resolution thermal mapping using a flexible platform of patterned quantum sensors. *Nano Lett.* **18**, 4684–4690 (2018).

253. von Kugelgen, S. & Freedman, D. E. A chemical path to quantum information. *Science* **366**, 1070–1071 (2019).

254. Bayliss, S. L. et al. Optically addressable molecular spins for quantum information processing. *Science* **370**, 1309–1312 (2020).

255. George, R. E., Edwards, J. P. & Ardavan, A. Coherent spin control by electrical manipulation of the magnetic anisotropy. *Phys. Rev. Lett.* **110**, 027601 (2013).

256. Trusheim, M. E. et al. Transform-limited photons from a coherent tin-vacancy spin in diamond. *Phys. Rev. Lett.* **124**, 023602 (2020).

257. Rose, B. C. et al. Strongly anisotropic spin relaxation in the neutral silicon vacancy center in diamond. *Phys. Rev. B* **98**, 235140 (2018).

258. Lo Nardo, R. et al. Spin relaxation and donor-acceptor recombination of Se$^+$ in 28-silicon. *Phys. Rev. B* **92**, 165201 (2015).

259. Lim, H.-J., Welinski, S., Ferrier, A., Goldner, P. & Morton, J. J. L. Coherent spin dynamics of ytterbium ions in yttrium orthosilicate. *Phys. Rev. B* **97**, 064409 (2018).

260. Mrózek, M. et al. Longitudinal spin relaxation in nitrogen-vacancy ensembles in diamond. *EPJ Quantum Technol.* **2**, 22 (2015).

261. Simin, D. et al. Locking of electron spin coherence above 20 ms in natural silicon carbide. *Phys. Rev. B* **95**, 161201 (2017).

262. Chaim, R. Relations between flash onset-, Debye-, and glass transition temperature in flash sintering of oxide nanoparticles. *Scr. Mater.* **169**, 6–8 (2019).

263. Agne, M. T., Hanus, R. & Snyder, G. J. Minimum thermal conductivity in the context of diffusion-mediated thermal transport. *Energy Environ. Sci.* **11**, 609–616 (2018).

264. Sun, Z., Li, M. & Zhou, Y. Thermal properties of single-phase Y$_2$SiO$_5$. *J. Eur. Ceram. Soc.* **29**, 551–557 (2009).

265. Cline, C. F., Dunegan, H. L. & Henderson, G. W. Elastic constants of hexagonal BeO, ZnS, and CdSe. *J. Appl. Phys.* **38**, 1944–1948 (1967).

266. Jones, G. H. S. & Hallett, A. C. H. The specific heat of crystalline quartz between 2 °K and 4 °K. *Can. J. Phys.* **38**, 696–700 (1960).

267. Wolfowicz, G. *Quantum Control of Donor Spins in Silicon and Their Environment*. PhD thesis, Oxford Univ. (2015).

268. Wandel, M. E. *Attenuation in Silica-based Optical Fibers*. Thesis, Tech. Univ. Denmark (2006).

269. Strehlow, W. H. & Cook, E. L. Compilation of energy band gaps in elemental and binary compound semiconductors and insulators. *J. Phys. Chem. Ref. Data* **2**, 163–200 (1973).

270. Ching, W. Y., Ouyang, L. & Xu, Y.-N. Electronic and optical properties of Y$_2$SiO$_5$ and Y$_2$Si$_2$O$_7$ with comparisons to α-SiO$_2$ and Y$_2$O$_3$. *Phys. Rev. B* **67**, 245108 (2003).

271. Brenneis, A. et al. Ultrafast electronic readout of diamond nitrogen–vacancy centres coupled to graphene. *Nat. Nanotechnol.* **10**, 135–139 (2014).

272. Ohno, K. *Nanometer-scale Engineering of Shallow Spins in Diamond*. PhD thesis, Univ. California, Santa Barbara (2014).